



HAL
open science

Wide-angle protostellar outflows driven by narrow jets in stratified cores

M. Rabenanahary, S. Cabrit, Z. Meliani, G. Pineau Des Forêts

► **To cite this version:**

M. Rabenanahary, S. Cabrit, Z. Meliani, G. Pineau Des Forêts. Wide-angle protostellar outflows driven by narrow jets in stratified cores. *Astronomy and Astrophysics - A&A*, 2022, 664, pp.A118. 10.1051/0004-6361/202243139 . hal-03652930

HAL Id: hal-03652930

<https://hal.science/hal-03652930>

Submitted on 18 Aug 2022

HAL is a multi-disciplinary open access archive for the deposit and dissemination of scientific research documents, whether they are published or not. The documents may come from teaching and research institutions in France or abroad, or from public or private research centers.

L'archive ouverte pluridisciplinaire **HAL**, est destinée au dépôt et à la diffusion de documents scientifiques de niveau recherche, publiés ou non, émanant des établissements d'enseignement et de recherche français ou étrangers, des laboratoires publics ou privés.

Wide-angle protostellar outflows driven by narrow jets in stratified cores

M. Rabenanahary¹, S. Cabrit^{1,2}, Z. Meliani³, and G. Pineau des Forêts^{1,4}

¹ Observatoire de Paris, PSL University, Sorbonne Université, CNRS, LERMA, 75014 Paris, France
e-mail: mi.aly.rabenanahary@obspm.fr

² Université de Grenoble Alpes, CNRS, IPAG, 38000 Grenoble, France

³ Observatoire de Paris, PSL University, Université de Paris, CNRS, LUTH 5 Place Jules Janssen, 92190 Meudon, France

⁴ Université Paris-Saclay, CNRS, Institut d'Astrophysique Spatiale, 91405 Orsay, France

Received 17 January 2022 / Accepted 31 March 2022

ABSTRACT

Most simulations of outflow feedback on star formation are based on the assumption that outflows are driven by a wide angle “X-wind,” rather than a narrow jet. However, the arguments initially raised against pure jet-driven flows were based on steady ejection in a uniform medium, a notion that is no longer supported based on recent observations. We aim to determine whether a pulsed narrow jet launched in a density-stratified, self-gravitating core could reproduce typical molecular outflow properties, without the help of a wide-angle wind component. We performed axisymmetric hydrodynamic simulations using the MPI-AMRVAC code with optically thin radiative cooling and grid refinement down to 5 au, on timescales up to 10 000 yr. Then we computed the predicted properties for the purposes of a comparison with observational data. First, the jet-driven shell expands much faster and wider through a core with steeply decreasing density than through an uniform core. Second, when blown into the same singular flattened core, a jet-driven shell shows a similar width as a wide-angle wind-driven shell in the first few hundred years, but a decelerating expansion on long timescales. The flow adopts a conical shape, with a sheared velocity field along the shell walls and a base opening angle reaching up to $\alpha \approx 90^\circ$. Third, at realistic ages of $\sim 10\,000$ yr, a pulsed jet-driven shell shows fitting features along with a qualitative resemblance with recent observations of protostellar outflows with the Atacama Large Millimeter Array, such as HH46-47 and CARMA-7. In particular, similarities can be seen in the shell widths, opening angles, position-velocity diagrams, and mass-velocity distribution, with some showing a closer resemblance than in simulations based on a wide-angle “X-wind” model. Therefore, taking into account a realistic ambient density stratification in addition to millenia-long integration times is equally essential to reliably predict the properties of outflows driven by a pulsed jet and to confront them with the observations.

Key words. stars: formation – stars: pre-main sequence – methods: numerical – ISM: jets and outflows – shock waves – hydrodynamics

1. Introduction

The most spectacular, and often the first observed, signature of the birth of a new star is the formation of a slow bipolar outflow of molecular gas. This phenomenon starts in the early protostellar phase of stellar mass assembly (Class 0), persists during the envelope dispersion phase (Class 1), and is ubiquitous across all masses (for a review, see e.g., Frank et al. 2014). Given their large sizes and high mass and momentum fluxes, ubiquity, and duration, molecular outflows are believed to play a key role in star formation on both small and large scales: recent numerical simulations (see e.g., Krumholz & Federrath 2019, for a review) suggest that they could be the main feedback agent setting the final stellar mass and core-to-star efficiency (via the removal of parent core material), and regulating the IMF peak, multiplicity fraction, and star formation efficiency at cluster scales (via the disruption of infall streams and replenishment of turbulence).

The exact effect of outflow feedback, however, depends on the assumed structure for the “primary” protostellar wind sweeping up the slow outflow. Two wind models are currently in use, both involving a fast and dense jet along the flow axis (as commonly observed in atomic or molecular tracers, see Frank et al. 2014) but strongly differing in the momentum injected at wider angles.

The first and most frequently used wind prescription in feedback simulations is that of Matzner & McKee (1999, hereafter MM99). It assumes a wide-angle wind radially expanding at a constant speed ($\approx 100\text{ km s}^{-1}$) over all angles, with a steep density increase towards the axis responsible for the appearance of an axial “jet.” This asymptotic structure was first derived for an “X-wind” magnetically launched from the disk inner edge (Shu et al. 1995) and only applies to hydromagnetic winds launched radially from a narrow region (MM99). Towards the equator, the wind momentum flux is still a sizeable fraction of the isotropic wind case¹ and can directly impact equatorial infall.

The second wind model, motivated by more recent MHD simulations and observations, assumes that the fast axial jet is surrounded by a slower disk wind, ejected within a limited solid angle (Federrath et al. 2014; Rohde et al. 2019). Feedback is then dominated by the jet, with much lesser impact on equatorial regions than in the MM99 prescription. Time variability in the form of episodic outbursts was also shown to affect outflow feedback (Rohde et al. 2019).

In principle, realistic MHD simulations of protostellar wind launching should provide the best wind prescription to adopt. However, the simulated wind structure depends on complex

¹ The fraction is $1/\ln(2/\theta_0) \approx 1/5$ for a “jet” collimation angle $\theta_0 \approx 0.01$ rad, cf. Eq. (2) in MM99.

effects that are still the subject of intense research and debate, such as the magnetosphere-disk interaction, the distribution of magnetic flux retained in the disk long after its formation, the turbulent viscosity and resistivity, and non-ideal effects (see e.g., Ireland et al. 2021; Ferreira & Deguiran 2013; Béthune et al. 2017).

An independent approach to determining the most realistic wind model for outflow feedback studies is to simulate the swept-up outflow properties on protostellar core scales ≤ 0.1 pc (where the ambient density structure is dominated by self-gravity and not yet perturbed by cloud inhomogeneities) and see which wind model best reproduces the observed outflow shapes and kinematics. Such a comparison was performed early on for two extremes in wind collimation: the wide-angle X-wind model (Shu et al. 1995; Matzner & McKee 1999) and a pure jet driving the outflow through large bowshocks (Masson & Chernin 1993; Raga & Cabrit 1993). Successes and caveats were identified in each case, based on early observations (see Cabrit et al. 1997; Lee et al. 2001; Arce et al. 2007) and these are briefly summarized and updated below.

First, in models of outflows driven by a wide-angle X-wind, the ambient medium is assumed to have a steep $1/r^2$ density decrease and a moderate degree of magnetic flattening. It is, in addition, assumed to mix instantaneously with shocked wind material. The swept-up shell then expands radially in a self-similar fashion that can reproduce several observed features of molecular outflows: “Hubble-law” kinematics $V \propto z$, mass-velocity distribution with a power-law slope $\gamma \approx -2$ (before opacity correction), and parabolic shapes with a wide base opening angle (Shu et al. 1991; Li & Shu 1996; Lee et al. 2001; Shang et al. 2006, 2020). An intrinsic caveat of this model, however, is that the uniform wind speed over all angles predicts much flatter internal shocks than observed in shock-excited H_2 along outflow axes. The observed curved H_2 bows requires a sharp drop of wind ram pressure away from the axis (see discussions in Lee et al. 2001; Arce et al. 2007).

Second, simulations of jet-driven bowshocks, in contrast, reproduce the curved morphology of internal shock fronts seen in H_2 very well (e.g., Suttner et al. 1997; Völker et al. 1999) as well as the associated “spur-like” features in CO (Lee et al. 2000). They can also reproduce the observed mass-velocity relations (Downes & Cabrit 2003; Moraghan et al. 2008) and apparent “Hubble-laws” when the jet is variable and precessing (Völker et al. 1999; Rohde et al. 2019). The jet-driven model for outflows was strongly criticized, however, for predicting too highly elongated cavities on long timescales (Ostriker et al. 2001), too much overlapping blueshifted and redshifted emission over a wide range of inclinations (Lee et al. 2001) as well as overly low velocities ≈ 0.03 km s $^{-1}$ when the bowshock had expanded to typical outflow widths of 10 000 au (Arce et al. 2007). As a result, it is commonly believed that jets alone cannot explain outflows with a wide opening angle, as reported for several evolved Class 1 protostars.

In order to combine the strengths of each model, a “dual wind” structure has been invoked with both a fast jet and a slower wide angle wind, where the latter would increasingly dominate at later times (Yu et al. 1999; Velusamy & Langer 1998; Arce et al. 2007; Zapata et al. 2014). There are several good reasons, however, to reconsider pure jet-driven shells as the potential origin for molecular outflows.

First, the critiques of Ostriker et al. (2001) and Lee et al. (2001) were based on models of jet-bowshocks in a uniform, or quasi-uniform, ambient medium (with at most a factor of 2 in density variation over the computational domain). In contrast,

a steep radial $1/r^2$ density decrease is assumed in wide-angle wind-driven models to yield the apparent “Hubble-law” acceleration (Shu et al. 1991; Lee et al. 2001). Such a decrease is expected on protostellar core scales ≤ 0.1 pc as a result of self-gravity. Raga & Cabrit (1993) and Cabrit et al. (1997) showed that it could produce a wider opening angle for jet-driven shells, more similar to observed flows, a result confirmed for steady jets on < 1000 yr timescales by Moraghan et al. (2008). Now that a steep density stratification is widely confirmed by observations of protostellar cores (e.g., van der Marel et al. 2009, for HH46-47) and that computational capabilities have greatly improved, it is important to explore the predicted effect on jet-driven shells over a broader parameter space and longer timescales than was feasible in the early study of Moraghan et al. (2008).

Second, the issue raised by Arce et al. (2007) related to insufficient bowshock speed at large widths no longer applies with a pulsed jet. New internal bowshocks generated by the jet variability will replenish a slow jet-driven shell with faster material at observable speeds (Raga & Cabrit 1993; Völker et al. 1999). In addition, the interaction between successive bowshocks will decrease their transverse speed, possibly alleviating the excessive blue and red overlap predicted at early times by Lee et al. (2001). Recent Atacama Large Millimeter Array (ALMA) observations revealed multiple H_2 bowshocks along outflow axes, connected to nested CO cavities along their flanks (e.g., HH212 and HH46-47 in Lee et al. 2015; Zhang et al. 2016). While some have been modeled with wind-driven shells (Zhang et al. 2019), it is important to have similar predictions for nested jet bowshocks at realistic ages $\approx 10^4$ yr.

Third, recent observational studies show that CO outflows are more elongated and collimated than initially thought: cloud-wide CO maps, as well as optical and infrared imaging surveys, show that at least 40% of outflows are more than a parsec long (Frank et al. 2014, and references therein). A striking example is the B5-IRS1 outflow, driven by a Class 1 protostar. While it exhibits a (projected) full opening angle $\alpha \approx 100^\circ$ at its base, argued as evidence for a wide-angle wind, unbiased CO maps of its parent cloud reveal that each lobe extends (at least) up to 2.2 pc from the source (Arce et al. 2010). The length-to-width ratio is then $q > 11$ (see maps in Frank et al. 2014). This is inconsistent with current models of shells driven by a wide angle X-wind (which predict an aspect ratio $q < 3.5$ for a base opening angle $\alpha \geq 70^\circ$, see Table 2 in Shang et al. 2020). The parsec size of many outflows appears more suggestive of jet-driven flows.

Estimated outflow opening angles are also affected by several biases: angular resolution, the height at which they are measured (Velusamy & Langer 1998; Velusamy et al. 2014), and inclination (angles appear wider in flows seen closer to pole-on). Two recent studies in Orion minimize these biases by providing uniform measurements at the same (high) linear resolution and projected height over randomly selected samples. In an ALMA survey of the widths of 22 (mostly Class 0) CO outflows (Dutta et al. 2020), 50% subtend projected full-opening angles in the range $\alpha = 25^\circ - 65^\circ$ at a projected altitude $z_{\text{proj}} = 800$ au. In a sample of 29 older outflow cavities (mostly Class 1) imaged in scattered light with HST (Habel et al. 2021), we see that 50% are in the range $\alpha = 8^\circ - 46^\circ$ at $z_{\text{proj}} = 8000$ au, and the fraction of point sources (viewed down the cavity interior) suggests a maximum deprojected opening angle $\alpha_{\text{deproj}} \leq 70^\circ$. Therefore, CO outflows seem to be more collimated on average than previously believed and it is necessary to investigate whether a pure jet (in a stratified core) could reproduce typical observed widths, before drawing any conclusions on a dominant contribution from a wider angle wind.

Here, we examine this issue by presenting the first high-resolution simulations of pure jet-driven shells in strongly stratified cores, up to ages of 10 000 yr and physical scales of 0.1 pc. For the first time in jet simulations, we consider the same flattened core structure as in the competing model of outflow driven by a wide-angle X-wind (Li & Shu 1996; Lee et al. 2001). We show that pulsed conical jets propagating in this environment sweep up a wider outflow cavity than in a uniform medium, with a width and opening angle that are compatible with recent outflow surveys. The predicted position-velocity diagrams and mass-velocity relation also show a promising qualitative agreement with recent ALMA outflow observations at high resolution and sensitivity, without any of the caveats noted previously for jet bowshocks in uniform media.

In Sect. 2, we present our numerical method and generic set up. In Sect. 3, we present the effect of a 1D and 2D density stratification on a jet-driven shell. In Sect. 4, we introduce a small jet opening angle and explore the effect of various free parameters on the cavity shape and kinematics. In Sect. 5, we present a simulation up to 10 000 yr and compute predicted flow widths, position-velocity diagrams, and mass-velocity relation, finding excellent qualitative agreement with recent ALMA observations. Section 6 summarizes our main results and conclusions.

2. General numerical setup

2.1. Governing equations, code, and numerical method

We performed axisymmetric 2D hydrodynamic simulations in cylindrical coordinates (R, z) , using the Message Passing Interface-Adaptive Mesh Refinement Versatile Advection Code (MPI-AMRVAC; Keppens et al. 2021). The hydrodynamics module of this finite volume, cell-centered code solves the hydrodynamic equations of mass, momentum, and energy conservation described, respectively, by:

$$\frac{\partial \rho}{\partial t} + \nabla \cdot (\rho \mathbf{v}) = 0, \quad (1)$$

$$\frac{\partial (\rho \mathbf{v})}{\partial t} + \nabla \cdot (\rho \mathbf{v} \mathbf{v}) + \nabla p = \mathbf{F}_p, \quad (2)$$

$$\frac{\partial e}{\partial t} + \nabla \cdot (e \mathbf{v} + p \mathbf{v}) = -n_{\text{H}}^2 \Lambda(T), \quad (3)$$

where ρ is the mass density, \mathbf{v} is the velocity vector, p is the thermal pressure, and $e = p/(\gamma - 1) + \rho \mathbf{v}^2/2$ is the total (thermal and kinetic) energy density, with γ the adiabatic index (taken here as 5/3). Two source terms are introduced on the right-hand side: following Lee et al. (2001), an inward-directed force field, $\mathbf{F}_p = \nabla p(t = 0)$, is imposed to maintain the unperturbed stratified ambient core in hydrostatic equilibrium at any time. In addition, optically thin equilibrium radiative cooling is included as a source term $-n_{\text{H}}^2 \Lambda(T)$ in the energy equation, with n_{H} the number density of hydrogen nuclei and T the gas kinetic temperature (van Marle & Keppens 2011). We consider an atomic gas with a standard helium fraction $x(\text{He}) = n(\text{He})/n_{\text{H}} = 0.1$, such that $n_{\text{H}} = \rho/(1.4m_{\text{H}})$ with m_{H} the mass of a proton. The temperature is inferred from gas pressure using the perfect gas law, $T = p/(n_{\text{tot}}k_{\text{B}})$, with n_{tot} as the total number of particles per unit volume. Given the moderate shock speeds encountered in our simulation, we assume that hydrogen and helium remain mostly neutral, so that $n_{\text{tot}} \approx n(\text{H}) + n(\text{He}) = 1.1n_{\text{H}}$. The cooling curve $\Lambda(T)$ depends on the local temperature, T , and the gas metallicity. Here, we use an atomic cooling curve with solar metallicity. In Sect. 3, we use for comparison purposes the

same cooling function as Lee et al. (2001), namely the curve of MacDonald & Bailey (1981) at temperatures above 10^4 K and Dalgarno & McCray (1972) below 10^4 K (with an ionization fraction $x_{\text{ion}} = 10^{-3}$). In the rest of the paper (Sects. 4 and 5) we keep the same low-temperature cooling curve but we adopt above 10^4 K the updated cooling function $\Lambda_{\text{HD}}(T)$ from Schure et al. (2009) generated with the SPEX code (Kaastra & Mewe 2000), which takes into account more up-to-date atomic parameters than MacDonald & Bailey (1981). In each simulation, the minimum temperature for radiative cooling is set at the initial ambient core temperature. This prevents the non-realistic radiative cooling of unshocked material inside the jet beam and the ambient core.

To solve Eqs. (1)–(3), we chose a Harten–Lax–van Leer contact (HLLC) scheme (Li 2005) with a minmod limiter. This combination is extremely robust in handling the shocks encountered in our problem.

As for the boundary conditions, the jet axis ($R = 0$) is treated as an axisymmetric boundary; the boundary conditions at $z = 0$ are fixed inside the jet inlet ($R < R_j$) and open in the surrounding ambient core. The outer limits of the computational domain are treated as open boundaries. The jet inlet (inside which the density and velocity vectors are prescribed at each time step) is a conical domain of radius $R = R_j$ at $z = 0$, height z_i , and semi-open angle θ_j .

Due to the high dynamic ratio between inner jet shock scale and propagation scales studied in this paper, it is crucial to use adaptive mesh refinement (AMR) to resolve the shocks in a cost-effective manner. Apart from Sect. 3 (where we use the same fixed grid resolution as Lee et al. 2001 for comparison purposes), all simulations performed in this paper have a base grid that is allowed to be locally refined up to four times, doubling the resolution at each new level of refinement (i.e., with a highest grid resolution at level 5 that is 2^4 finer than at level 1). The refinement-derefinement criterion is based on a Lohner error estimator on the quantity $n_{\text{H}}^2 \Lambda(T)$. We further ensure that the highest level of refinement is always present inside the jet beam.

2.2. Velocity variability of the jet

Pulsed jets are simulated by time-varying the jet velocity around its initial value v_0 , as

$$v_j(t) = \|\mathbf{v}_j(t)\| = v_0 h(t), \quad (4)$$

where $h(t)$ is the dimensionless variability profile defining how the jet will pulse.

Following Lee et al. (2001), we keep the jet mass-flux constant over time in the present paper, by imposing an inverse variation of the jet density:

$$\rho_{j0}(t) = \frac{\rho_{j0}}{h(t)} = \frac{\rho_{j0}v_0}{v_j(t)}, \quad (5)$$

where ρ_{j0} is the initial jet density at $z = 0$, $R = R_j$, and $t = 0$.

2.3. Tracers

Following Porth et al. (2014), the code also solves the advection equation of two passive fluid tracers, **tracer_a** and **tracer_j**, which trace fluid parcels originating from the ambient core and from the jet, respectively. They evolve according to:

$$\frac{\partial \text{tracer}_k}{\partial t} + \mathbf{v} \cdot \nabla \text{tracer}_k = 0, \text{ for } k = a, j. \quad (6)$$

Table 1. Parameters of the pulsed cylindrical jet simulations (Sect. 3).

Fixed parameters (from Lee et al. 2001)				
One-sided jet mass-loss rate	$\dot{M} = 6.0 \times 10^{-8} M_{\odot} \text{ yr}^{-1}$			
Jet semi-opening angle	$\theta_j = 0^{\circ}$			
Jet radius	$R_j = 2.5 \times 10^{15} \text{ cm}$			
Mean jet velocity	$v_0 = 120 \text{ km s}^{-1}$			
Jet velocity variation	$v_j(t) = v_0 + \Delta V \sin \frac{2\pi t}{P}$			
Semi-amplitude	$\Delta V = 60 \text{ km s}^{-1}$			
Jet density variation	$\rho_j(t) = \rho_{j0} [v_0/v_j(t)]$ (constant mass-flux)			
Jet density at $t = 0$	$\rho_{j0} = 1.6 \times 10^{-20} \text{ g cm}^{-3}$			
Jet temperature	$T_j = 270 \text{ K}$			
Ambient core temperature	$T_a = 30 \text{ K}$			
Radiative cooling function	$\Lambda(270 \text{ K} \leq T < 10^4 \text{ K})$ from Dalgarno & McCray (1972) $\Lambda(T \geq 10^4 \text{ K})$ from MacDonald & Bailey (1981)			
Simulation domain	$(R, z) = (7.0 \times 10^{16} \text{ cm}, 1.4 \times 10^{17} \text{ cm}) = (4679 \text{ au}, 9358 \text{ au})$			
Number of cells	$n_R \times n_z = 336 \times 672$			
Resolution	$\Delta R = \Delta z = 2.08 \times 10^{14} \text{ cm} = 14 \text{ au}$			
Variable parameters				
Model name	PCJ-U ^(a) (Fig. 1a)	PCJ-Z (Fig. 1b)	PCJ-R (Fig. 1c)	PCJ-RW ^(b) (Fig. 2)
Core density profile	Uniform	z -stratified	Flattened singular core	
$\rho_a(\mathbf{r})$	ρ_{a0}	$\rho_{a0} \left(1 + \frac{z}{z_c}\right)^{-2}$ $z_c = 10^{16} \text{ cm}$	$\rho_{a0} \sin^2 \theta r_0^2 (R^2 + z^2)^{-1}$ $r_0 = 2.5 \times 10^{15} \text{ cm}$	
Core density at $z = 0, R = 2.5 \times 10^{15} \text{ cm}$	$\rho_{a0} = 1.6 \times 10^{-20} \text{ g cm}^{-3}$		$1.6 \times 10^{-18} \text{ g cm}^{-3}$	
Core/jet density contrast at $z = 0$	$\eta = \rho_{j0}/\rho_{a0} = 1$		0.01	
Jet variability period	$P = 310 \text{ yr}$		115 yr	
Simulation age	$t = 610 \text{ yr}$		296 yr	

Notes. ^(a)Identical parameters to pulsed jet simulation of Lee et al. (2001) (see their Fig. 7). ^(b)Identical parameters to pulsed wind simulation of Lee et al. (2001) (cf. their Fig. 12), except that the wide-angle wind is replaced here by a cylindrical jet of same mass-flux, injection radius, and velocity variability.

These tracers are dimensionless numerical quantities. To improve numerical precision and accurately track mixing between the jet and ambient core material, they are taken to cover a wide range $[0, 10^7]$. Thus, at $t = 0$, **tracer**_{*j*} (resp. **tracer**_{*a*}) is initialized to 10^7 inside the jet beam (resp. the surrounding core) and is set to zero elsewhere.

From those tracers, we may compute the local fraction of material originating from the ambient core and from the jet, f_a and f_j , inside each mesh cell and at any time step, as

$$f_k = \frac{\text{tracer}_k}{\text{tracer}_a + \text{tracer}_j}, \text{ for } k = a, j. \quad (7)$$

3. Pulsed cylindrical jet in a non-uniform medium

In this section, we investigate how the shape of the shell driven by the same cylindrical jet as in Lee et al. (2001) is influenced by a more realistic, steep density decrease in the ambient core (Sect. 3.2). We then compare with the wide-angle wind-driven shell modeled in Lee et al. (2001) for the same age and core stratification (Sect. 3.3).

3.1. Setup and choice of density stratifications

To make a comparison with Lee et al. (2001), we adopted their pulsed cylindrical jet model (thereafter PCJ) with the same jet

radius, R_j , temperature, T_j , sinusoidal variation of jet velocity, $v_j(t)$, inversely varying jet density, $\rho_j(t)$, and constant one-sided jet mass-loss rate, \dot{M} . We also adopted the same uniform spatial resolution of 14 au, radiative cooling law (using MacDonald & Bailey 1981 above 10^4 K), domain size, ambient temperature, and simulation ages. The particular setup presented in this section is summarized in Table 1.

We then investigated three different ambient core stratifications: first, just as in the jet-driven simulations of Lee et al. (2001), we considered a uniform core, with

$$\rho_a(R, z) = \rho_{a0}. \quad (8)$$

Second, we investigated a z -stratified core following the prescription in Cabrit et al. (1997):

$$\rho_a(R, z) = \rho_{a0} \left(1 + \frac{z}{z_c}\right)^{-2} \text{ with } z_c = 10^{16} \text{ cm}, \quad (9)$$

where the value of z_c is justified by observations of protostellar cores showing a steep stratification from 20 000 au down to (at least) 1000 au (see e.g., Motte & André 2001; van der Marel et al. 2009). Lee et al. (2001) investigated (see their Sect. 3.6) a somewhat similar z -stratification $\rho_a(z) \propto 1/[1 + (z/z_c)^2]$ but with a flattening scale $z_c = 1.25 \times 10^{17} \text{ cm}$ that is ten times greater than in Eq. (9) and equal to the size of their computational box. The ambient density thus dropped only by a factor of 2 across

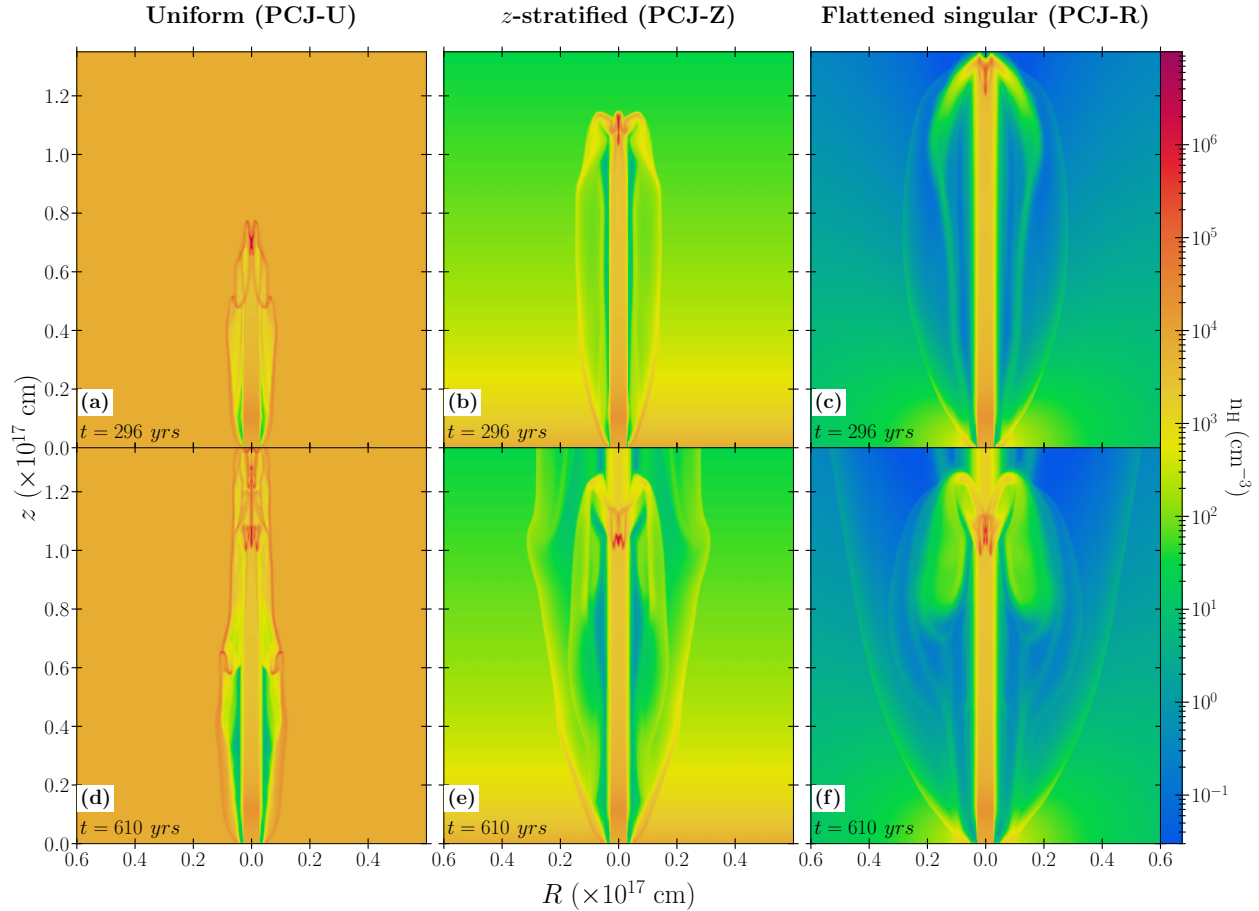


Fig. 1. Maps of hydrogen nuclei density n_{H} from simulations of the same cylindrical jet as in Lee et al. (2001) (see Table 1). The three columns confront three different ambient core stratifications, and the two rows show the map at two ages $t = 296$ yr (top) and 610 yr (bottom). The jet is launched in Figs. 1a and d through a uniform ambient core with profile $\rho(R, z) = \rho_{a0}$; in Figs. 1b and e through an z -stratified ambient core $\rho(R, z) = \rho_{a0}/(1 + z/z_c)^2$ with $z_c = 10^{16}$ cm; and in Figs. 1c and f through a flattened singular core $\rho(r, \theta) = \rho_{a0} \sin^2 \theta (r_0/r)^2$, where r is the spherical radius and $r_0 = 2.5 \times 10^{15}$ cm. All core density profiles have the same base density at $R = R_j$, $\rho_{a0} = 1.6 \times 10^{-20}$ g cm $^{-3}$, density-matched with the jet at $t = 0$. We note how the jet-driven shell expands faster and wider through an increasingly stratified core, whereas the nested shells grow wider.

the whole domain and no strong effect on shell morphology was reported.

Third, we considered the same flattened singular core profile as in the wide angle wind-driven simulations of Lee et al. (2001), namely:

$$\rho_a(r, \theta) = \rho_{a0} \sin^2 \theta \left(\frac{r_0^2}{r^2} \right) \quad \text{with} \quad r_0 = 2.5 \times 10^{15} \text{ cm}, \quad (10)$$

where $r = (R^2 + z^2)^{1/2}$ denotes the spherical radius and θ is the polar angle from the jet axis. This $1/r^2$ decrease is appropriate for a self-similar singular isothermal core. The $\sin^2 \theta$ dependence is an approximation for the flattened magnetostatic equilibrium solution of Li & Shu (1996) with $n = 2$ (where this parameter measures the degree of magnetic support and equatorial flattening). When a core is stratified according to this particular solution and is then swept-up by an X-wind, it can reproduce the typical collimation, parabolic shape, and mass-velocity distribution in CO outflows, while also being consistent with the mean observed flattening of prestellar cores (Li & Shu 1996). Hence, analytical models and numerical simulations of X-wind driven shells (Lee et al. 2000, 2001; Zhang et al. 2019) widely adopt the expression in Eq. (10) as a “standard” ambient medium.

However, to our knowledge, it was never used in jet-driven outflow simulations until now.

3.2. Effect of ambient core stratification on jet-driven shells

Figure 1 shows the results of our simulations at the same ages and for the same cylindrical jet propagating into three different density distributions: uniform (model PCJ-U, Figs. 1a and d), z -stratified (model PCJ-Z, Figs. 1b and e), and flattened singular core (model PCJ-R, Figs. 1c and f). All three have the same value of $\rho_{a0} = 1.6 \times 10^{-20}$ g cm $^{-3}$ in Eqs. (8), (9), and (10), respectively. Since $R_j = 2.5 \times 10^{15}$ cm = r_0 , the ambient density at the jet base ($z = 0, R = R_j$) is also the same in all three cases (equal to ρ_{a0}), as well as the initial ($t = 0$) jet-ambient density contrast $\eta = 1$ at this point. All model parameters are summarized in Table 1.

Going from left to right in Fig. 1, the ram pressure constraints exerted on both the main and nested shells are relaxed along the z -axis, and then along both the radial and polar directions. As we may see, this change leads to a main shell expanding faster along z and wider over time.

As already noted by Lee et al. (2001), we confirm that a uniform medium produces a narrow and roughly cylindrical jet-driven shell, unlike observed outflows. However, introducing a

steep $1/z^2$ stratification here leads to a more conical leading shell as time proceeds, confirming the analytical and numerical predictions of Raga & Cabrit (1993) and Cabrit et al. (1997). For example, at 610 yr, the shell full width at the top of the domain is increased by a factor 4 between PCJ-U and PCJ-Z (from 1.3×10^{16} cm to 5.6×10^{16} cm). In the flattened singular core PCJ-R, the rarefied polar holes create an even wider shell with a parabolic shape and a twice larger full width than in PCJ-Z (1.0×10^{17} cm).

Even though the ambient density at the jet inlet ($z = 0, R = R_j$) was kept the same, a steeper density stratification also increases the shell full width near its base. From Fig. 1, we can measure full widths at $z = 800$ au ($= 1.2 \times 10^{16}$ cm) of $W_{800} = 0.95 \times 10^{16}$ cm, 1.16×10^{16} cm and 1.75×10^{16} cm for the uniform medium, $1/z^2$ decrease and flattened singular core, respectively.

In addition to the leading shell carved by the supersonic jet head, jet variability produces successive and periodic internal working surfaces (thereafter IWS) where high-pressure shocked material is ejected sideways, forming bowshocks expanding inside the leading shell and producing nested “secondary” shells, visible in the $t = 610$ yr snapshot in Fig. 1. As the leading shell expands faster and wider in a stratified core, its inner density distribution (and, hence, the pressure locally exerted on the nested shells) drops more steeply than through an uniform core. This allows the nested shells to expand more widely as well. In parallel, each IWS still moves along the jet beam at the same velocity, independently of the core stratification. This is because the IWS propagation speed only depends on the jet velocity and density conditions upstream and downstream of the forming working surface (Raga et al. 1990). These conditions are entirely determined by the jet variability properties, which remain unmodified for each of our core density profiles.

3.3. Comparison with a wide-angle wind-driven shell

Here, we adopt the same setup as in PCJ-R (Figs. 1c, f), but with a flattened singular core that is 100 times denser and identical to that considered in the wide-angle wind models of Lee et al. (2001), with $\rho_{a,0} = 1.6 \times 10^{-18}$ g cm $^{-3}$. We also adopt a shorter variability period $P = 115$ yr than in Sect. 3.2, so that our pulsed cylindrical jet has the exact same mass-loss rate, injection radius, and velocity variability as their pulsed wide-angle wind. The parameters of this new model (PCJ-RW) are summarized in the last column of Table 1.

Figure 2 shows the resulting density map of the PCJ-RW simulation at an age $t = 296$ yr. This map can directly be compared with the wide-angle wind simulation at the same age in Fig. 12 of Lee et al. (2001). At this early age, the jet-driven shell opens as wide as for the pulsed wide-angle wind in the same ambient stratification; namely, we measure similar maximum shell widths of 2.6×10^{16} cm ($\sim 10 R_j$) for both models, and a similar full opening angle² at $z = 800$ au of $\alpha_{800} = 70^\circ$ for PCJ-RW and $\alpha_{800} = 80^\circ$ for the wide-angle wind model.

3.4. Summary

The usual criticism of jet-driven shells producing overly narrow opening angles appears no longer valid when a realistic stratified ambient medium is considered. The morphology of the shell

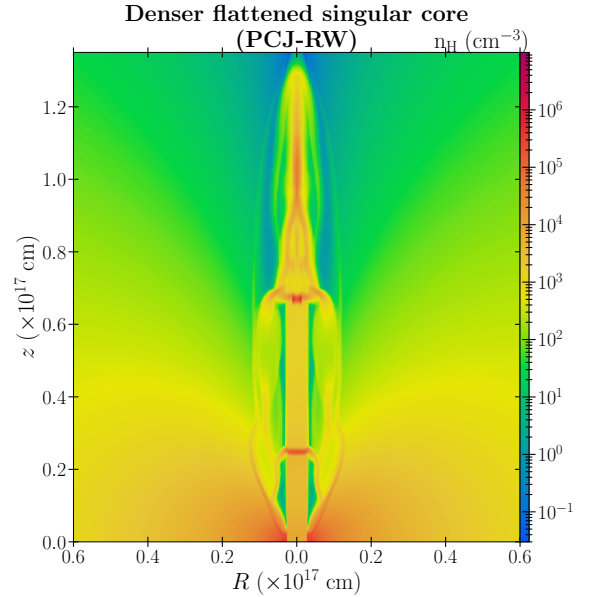


Fig. 2. Density snapshot at $t = 296$ yr of pulsed cylindrical jet model PCJ-RW, with same injected mass-loss rate, velocity variability, and ambient density distribution as the pulsed wide-angle wind model in Fig. 12 of Lee et al. (2001). The resulting shell size and opening angle are the same as for the wind-driven shell, at this young age.

driven by a pulsed jet is strongly affected by a steep stratification in density of the ambient core surrounding the jet. Wider shells are formed with increased opening angle near the base of the outflow and conical or parabolic shapes on large scales are highly reminiscent of observed CO outflows. Furthermore, in a standard flattened singular core, the jet-driven shell initially expands as wide as with a wide-angle wind. In the rest of this paper, we examine which factors affect the jet-driven shell shape (see Sect. 4) and how it evolves on longer timescales $\sim 10\,000$ yr, which more closely resemble the actual outflow ages (see Sect. 5).

4. Shells driven by a conical jet in a flattened singular core

In this section, we investigate the influence that several physical parameters (expected to vary among observed sources) have on the morphology and kinematics of jet-driven shells. For consistency, we keep the singular flattened core stratification in Eq. (10) (as in wide-angle wind-driven models), but we adopt a more realistic conical jet geometry. High-resolution jet observations suggest jet half-opening angles θ_j of a few degrees on the scales of our simulations, for example $\theta_j = 2^\circ$ out to 800 au in the atomic jet of RW Aur (Dougados et al. 2000) and $\theta_j \simeq 5^\circ$ from 1000–12 000 au in the CO jet of IRAS04166+2706 (Santiago-García et al. 2009). We explore a similar range in our simulations.

4.1. Setup: Jet spray nozzle, radiative cooling, and AMR

Similar to Völker et al. (1999), we introduce a spray angle in the jet inlet by taking a velocity vector that is radially diverging from a virtual point:

$$(R, z) = (0, -z_0), \quad \text{with } z_0 = R_j / \tan \theta_j, \quad (11)$$

² Defined following Dutta et al. (2020) as $\alpha_{800} = 2 \arctan(W_{800}/[2 \times 800 \text{ au}])$.

Table 2. Parameters of pulsed conical high-density jet simulations with the resulting opening angles and full widths (Fig. 3).

Fixed parameters						
Mean jet velocity	$v_0 = 120 \text{ km s}^{-1}$					
Jet density variation	$\rho_j(t) = \rho_{j0} [v_0/v_j(t)] \times (R_j^2 + z_0^2)(R^2 + [z + z_0]^2)^{-1}$, with $z_0 = R_j/\tan\theta_j$ (constant mass-flux)					
Core density profile	Flattened singular core $\rho_a(\mathbf{r}) = \rho_{a0} \sin^2\theta r_0^2 (r^2)^{-1}$, with $r_0 = 2.5 \times 10^{15} \text{ cm}$					
Jet temperature	$T_j = 100 \text{ K}$					
Ambient core temperature	$T_a = 100 \text{ K}$					
Radiative cooling function	$\Lambda(100 \text{ K} \leq T < 10^4 \text{ K})$ from Dalgarno & McCray (1972) $\Lambda(T \geq 10^4 \text{ K})$ from Schure et al. (2009)					
Simulation domain	$(R, z) = (7.0 \times 10^{16} \text{ cm}, 1.9 \times 10^{17} \text{ cm}) = (4679 \text{ au}, 12\,700 \text{ au})$					
Number of cells	$n_R \times n_z = 56 \times 152$ for the full grid at AMR level 1					
Maximum resolution	$7.8 \times 10^{13} \text{ cm} = 5.2 \text{ au}$ at AMR level 5					
Snapshot age	700 yr					
Parameter	Reference model H_REF	Modified parameter ^(a)	Modified Model name	α_{800} ^(b) ($^\circ$)	\mathbf{W}_{800} ^(c) (10^{16} cm)	\mathbf{W}_{12700} ^(d) (10^{16} cm)
Core base density ρ_{a0}	$1.6 \times 10^{-18} \text{ g cm}^{-3}$	$1.6 \times 10^{-20} \text{ g cm}^{-3}$	H_DENSA	112	3.5	13.8
Jet semi opening angle θ_j	3°	7°	H_THETA	95	2.6	10.5
Jet base initial density ^(e) ρ_{j0}	$1.8 \times 10^{-17} \text{ g cm}^{-3}$	$1.8 \times 10^{-15} \text{ g cm}^{-3}$	H_DENSJ	86	2.2	8.4
Semi-amplitude ΔV	60 km s^{-1}	90 km s^{-1}	H_VARAMP	91	2.4	8.0
Jet variability period P	115 yr	300 yr	H_PER	90	2.4	7.4
Jet variability profile $h(t)$	$1 + \frac{\Delta V}{v_0} \sin \frac{2\pi t}{P}$	$1 + \frac{\Delta V}{v_0} \{1 - 2 \cdot \text{mod}(\frac{t}{P}, 1)\}$	H_SAWT	86	2.2	7.2
Jet radius R_j	$7.5 \times 10^{14} \text{ cm}$	$3.0 \times 10^{14} \text{ cm}$	H_RAD	84	2.2	6.9

Notes. ^(a)In each modified model, only one parameter at a time is changed with respect to the reference model. ^(b)Shell full opening angle at $z = 800 \text{ au}$. We obtain $\alpha_{800} = 88^\circ$ for the reference model. ^(c)Full shell width at $z = 800 \text{ au}$. We obtain $\mathbf{W}_{800} = 2.3 \times 10^{16} \text{ cm}$ for the reference model. ^(d)Full shell width at $z = 12\,700 \text{ au}$ (top of the grid). We obtain $\mathbf{W}_{12700} = 7.6 \times 10^{16} \text{ cm}$ for the reference model. ^(e)High jet density case, yielding a one-sided mass-flux $\dot{M} = 6 \times 10^{-6} M_\odot/\text{yr}$ for the reference values of θ_j and R_j .

where R_j is the jet radius at $z = 0$ and θ_j the jet semi-opening angle.

In order to conserve mass-flux throughout the jet inlet, we set a jet density profile $\rho_j(t)$ that decreases as the inverse square distance to the above-mentioned virtual point and varies inversely in time with the velocity modulus, as

$$\rho_j(t) = \rho_{j0} \left(\frac{R_j^2 + z_0^2}{R^2 + (z + z_0)^2} \right) \frac{v_0}{v_j(t)}, \quad (12)$$

where ρ_{j0} is the jet ‘‘base density’’ at $z = 0$, $R = R_j$, and $t = 0$. The (constant) jet mass-flux is then given by

$$\dot{M} = 2\pi (1 - \cos\theta_j) (R_j^2 + z_0^2) \rho_{j0} v_0, \quad (13)$$

$$= 2\pi (1 - \cos\theta_j) (R_j/\sin\theta_j)^2 \rho_{j0} v_0. \quad (14)$$

Hereafter, and in Sect. 5, we use the updated radiative cooling function from [Schure et al. \(2009\)](#) (see Sect. 2.1). Furthermore, the resolution and accuracy are improved by enabling AMR up to level 5, with a 84 au minimal and 5.2 au maximal spatial resolution. The computational grid is also expanded to $1.9 \times 10^{17} \text{ cm}$ in z .

4.2. Model parameters

First, we defined a set of typical parameters for the reference models. For consistency, we kept the same ejection velocity law and ambient density distribution (singular flattened core) as in our model PCJ-RW in Table 1. We adopted a reference value

$\theta_j = 3^\circ$ for the jet semi-opening angle, and a reference jet radius $R_j = 50 \text{ au}$ at $z = 0$. As for the jet base density ρ_{j0} , we considered a ‘‘high-density’’ value, giving a one-sided jet mass-flux $\dot{M} = 6 \times 10^{-6} M_\odot \text{ yr}^{-1}$ typical of very active Class 0 protostars, for our reference values of θ_j and R_j .

We then launched seven modified models, each having only one parameter changed with respect to the reference model (H_REF):

- (i) H_DENSA: with an ambient density scaling $\rho_{a0} = 1.6 \times 10^{-20} \text{ g cm}^{-3}$ instead of $1.6 \times 10^{-18} \text{ g cm}^{-3}$;
- (ii) H_THETA: with a jet semi-opening angle $\theta_j = 7^\circ$ instead of 3° ;
- (iii) H_DENSJ: with a jet base density ρ_{j0} 100 times larger than the reference model;
- (iv) H_VARAMP: with a variability semi-amplitude $\Delta V = 90 \text{ km s}^{-1}$ instead of 60 km s^{-1} ;
- (v) H_PER: with a variability period $P = 300 \text{ yr}$ instead of 115 yr;
- (vi) H_SAWT: with a sawtooth velocity variability profile instead of a sinusoidal one;
- (vii) H_RAD: with an initial jet radius $R_j = 20 \text{ au}$ instead of 50 au.

We note that all the models have the same value of jet mass-flux as the reference model H_REF, except for H_THETA, H_DENSJ, and H_RAD, since \dot{M} independently varies with θ_j , ρ_{j0} , and R_j according to Eq. (13). All input parameters for the reference and modified models in this ‘‘high-density’’ case are summarized in Table 2.

To check the robustness of our conclusions, we also computed a second sequence of models with the same parameter

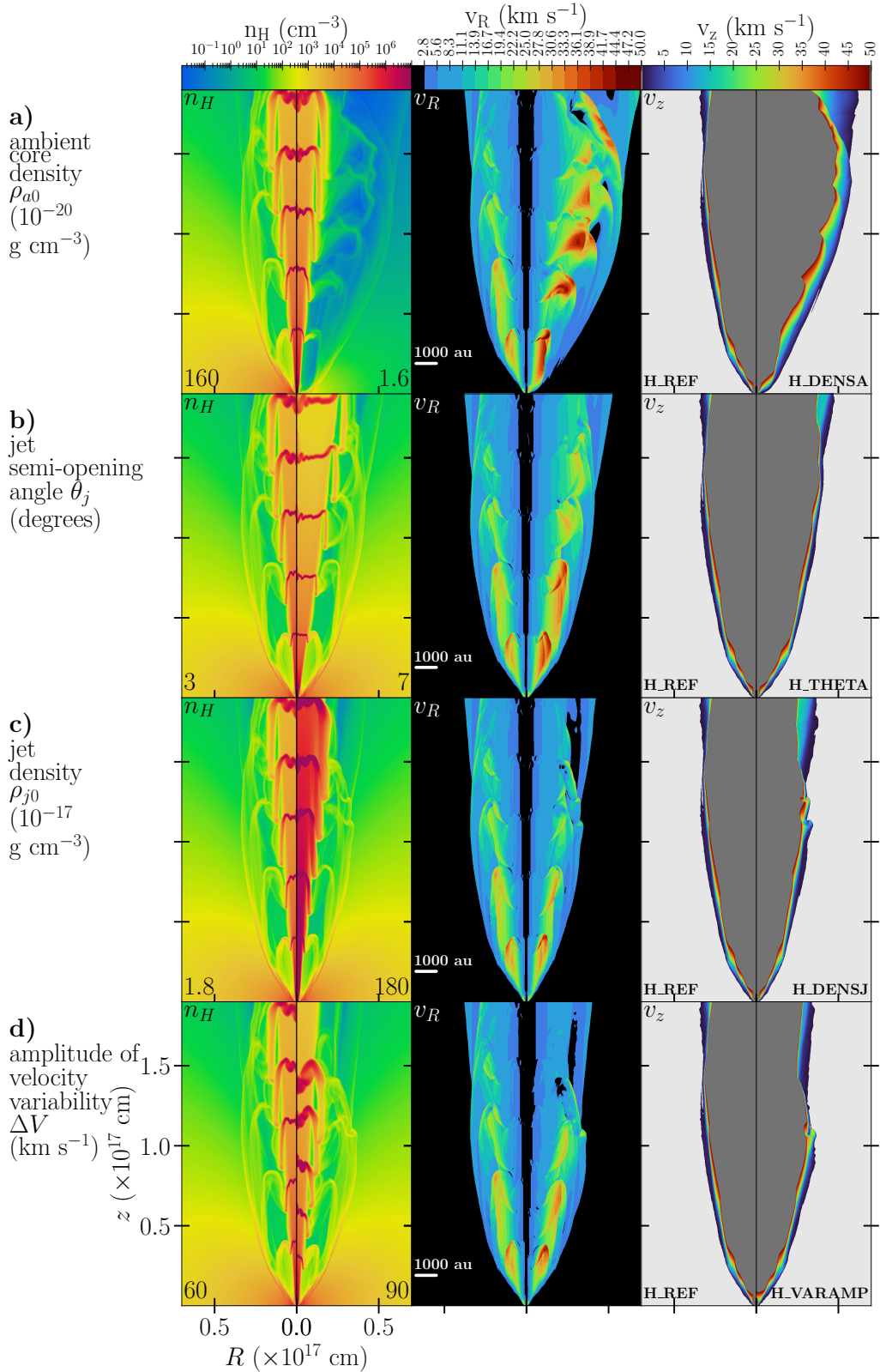


Fig. 3. Influence of seven free parameters on the geometry and kinematics of shells driven by a pulsed conical jet in a singular flattened core, at an age of $t = 700$ yr. Each row corresponds to a different free parameter (as labeled in the left margin) and compares maps of number density, n_H (left), radial velocity, v_R (middle), and axial velocity, v_z (right), for the reference model (left half of each map) and the modified model (right half of each map). The corresponding modified parameter values are marked at the bottom of the n_H panel and model names at the bottom of the v_z panel. Velocity colorbars are cropped to 0–50 km s $^{-1}$ for better visualization of the range detected in CO outflows. The reference model in this figure has a high mass-flux of $6 \times 10^{-6} M_{\odot} \text{yr}^{-1}$ (see Table 2 for full list of model parameters). The main effect on the cavity shape is seen when varying the core density.

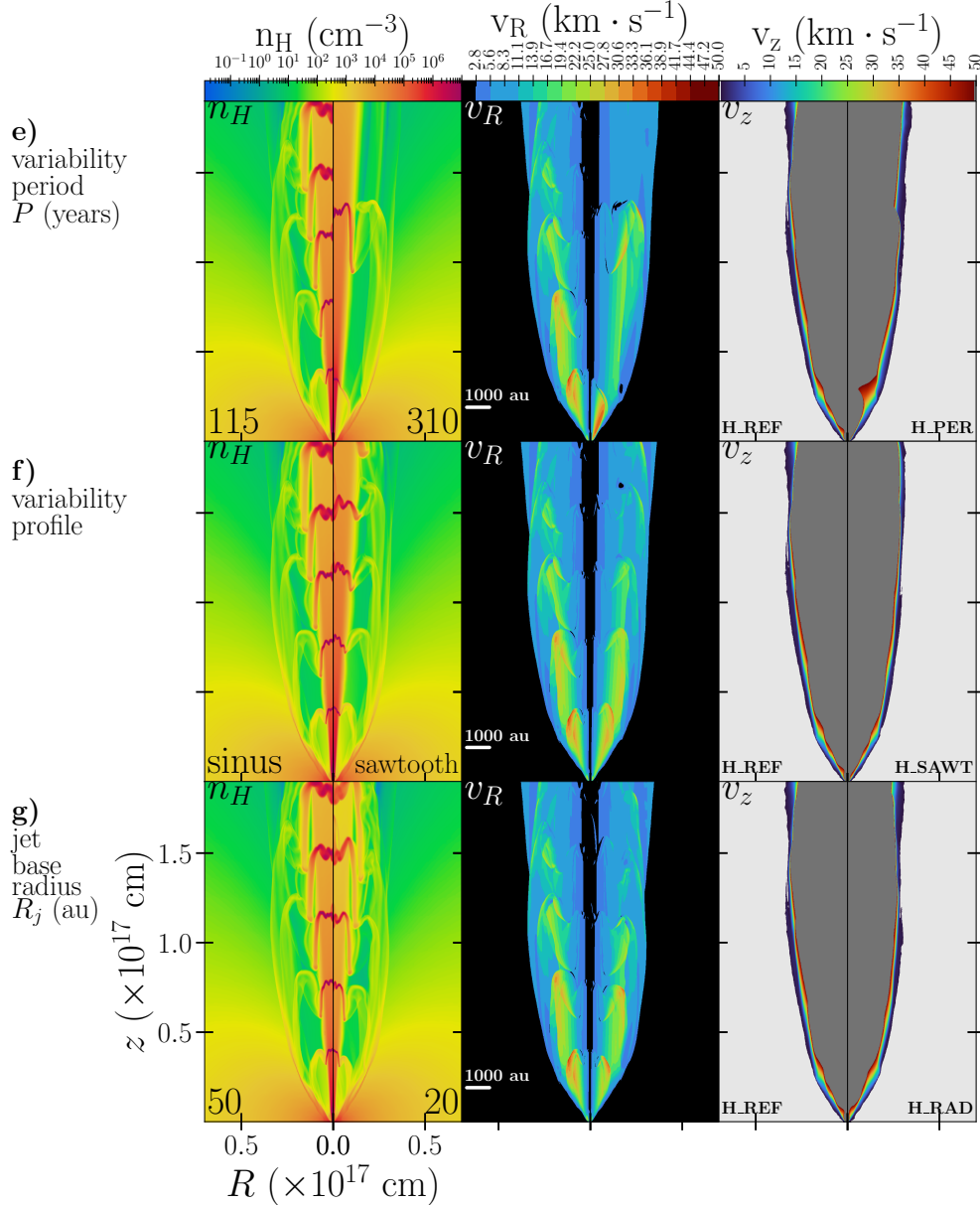


Fig. 3. continued.

changes, but with a 100 times smaller reference jet density. This leads to $\dot{M} = 6 \times 10^{-8} M_{\odot} \text{yr}^{-1}$ in the corresponding reference model (M_REF) that is typical of more evolved Class 1 jets. The parameters of this second sequence of models (referred to as the “medium-density” case) are summarized in Table A.1 and the results are summarized graphically in Fig. A.1.

4.3. Results

Figure 3 shows the differences in shape and kinematics of the shells between the reference and modified models in the high-density case, by comparing their respective maps of n_H (H nucleus number density), v_R , and v_z at the same age of $t = 700$ yr. The v_R maps show the lateral expansion induced by successive bowshocks, while the v_z maps highlight the shear-like velocity gradient that develops along the main shell walls.

For an easier comparison between models, we use the density maps in Fig. 3 to measure the full width $\mathbf{W}(z)$ of the main shell as a function of altitude z . We thus obtain Fig. 4 that overplots

the resulting shell shapes of each model. Finally, from the shell width \mathbf{W}_{800} at an altitude $z = 800$ au, we derive the full opening angle near the base, defined following Dutta et al. (2020) as $\alpha_{800} = 2 \arctan(\mathbf{W}_{800}/[2 \times 800 \text{ au}])$. Values of α_{800} , \mathbf{W}_{800} , and \mathbf{W}_{12700} (the full width at the top of the computational box) are summarized in the last three columns of Table 2.

The most impactful effect on both the morphology and kinematics of the main shell is obtained here when decreasing the core base density, ρ_{a0} , by a factor 100. In this case, Figs. 3a and 4 clearly show that the leading shell opens twice wider; v_R reaches higher values, which cover broader areas within the nested shells. The layer of strong v_z -gradient (between 0 and 50 km s^{-1}) along the main shell surface also becomes thicker.

Increasing the jet opening angle (Figs. 3b and 4) has a more moderate effect, with a maximum $\sim 30\%$ increase of the main shell full width in comparison with the reference model in the high-density case. Increasing the jet base density by a factor 100 also has a moderate influence (see Figs. 3c and 4).

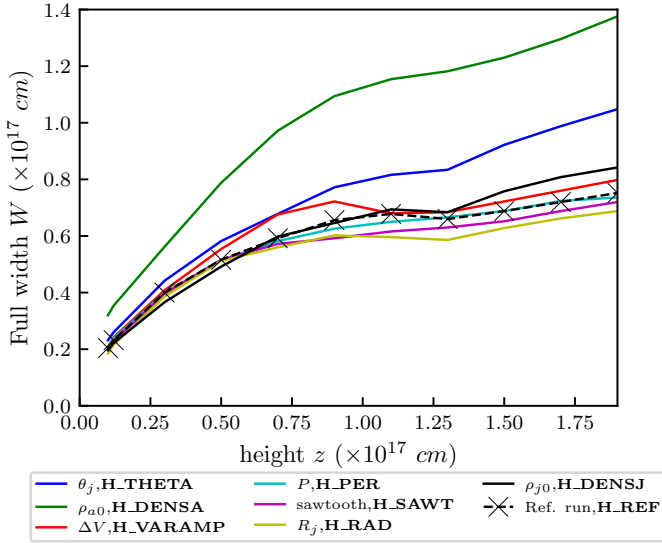


Fig. 4. Full shell width $W(z)$ at $t = 700$ yr as a function of altitude, z , for the high-density jet models in Fig. 3. Colored curves have one parameter varied from the reference run, from among the ambient core base density ρ_{a0} , jet semi-opening angle θ_j , initial jet base density ρ_{j0} , semi-amplitude of variability ΔV , period P , variability profile (sawtooth instead of sinusoidal), or jet radius R_j . Model parameter values are listed in Table 2. The covered measurements range from $z \sim 800$ au to $z \sim 12\,700$ au.

Finally, the shape and kinematics of the main shell are little affected when semi-amplitude ΔV (Fig. 3d), variability period P (Fig. 3e) are increased, when a sawtooth profile $h(t)$ is superimposed (Fig. 3f), or when the jet radius R_j (Fig. 3g) is decreased. However, we find that in comparison with the sinusoidal case, a sawtooth-like profile of variability leads to smoother shells borders and less unstable bowshocks and IWS, as well as reduced instabilities in general (cf. Fig. 3f).

We obtain the same behaviors for a reference jet density that is 100 times smaller (see Fig. A.1). Except for the ambient density, parameter changes only have modest effects on the shell width.

5. Millenia-long simulations of a conical pulsed jet in a stratified core

In this section, we investigate the long-term evolution of the shells driven by a pulsed conical jet through a flattened singular core. To do so, for the first time we present this type of simulation reaching up to 10 000 yr. Predicted sizes, position-velocity (PV) diagrams, and mass-velocity distributions are presented and qualitatively compared with the typical behavior in Atacama Large Millimeter/sub-millimeter Array (ALMA) observations of outflows.

5.1. Setup

In Sect. 4, we noted that a sawtooth jet velocity variability profile minimizes the development of instabilities without changing the overall shell shape and kinematics. We thus adopted such a sawtooth profile here, since it allows us to reach the desired long timescales at a more reasonable CPU cost. For consistency, we adopted the same jet and ambient parameters as in model M_SAWT in Table A.1, except for the variability period. We considered here a slightly longer value $P = 300$ yr, as inferred

from CO observations of both the HH46-47 outflow by Zhang et al. (2019) and the CARMA-7 outflow by Plunkett et al. (2015), before the inclination correction.

To keep a non-prohibitive computational time, we also use here a more diffusing Total Variation Diminishing Lax Friedrichs numerical scheme (TVDLF) at the shocks zone. This decreases the instabilities at the highest resolution, without changing the overall shell structure. Finally, to follow the outflow expansion, the computational domain is expanded to 3.0×10^{17} cm = 20 000 au in R and z ($n_R \times n_z = 240 \times 240$ cells at AMR level 1), keeping the same resolution as in Sect. 4 and Table 2.

5.2. Long-time maps of density, mixing fraction, and velocities

Figure 5 shows the distribution of number density, n_H , fraction of core-originated material, f_a , and orthoradial and axial velocities, v_R and v_z , in the outflow at $t = 10\,000$ yr. Figure 5a shows that after 10 000 yr, the outflow structure differs from that seen at earlier ages (e.g., in Fig. 3). The initially single shell has split into two separate shells: an “outer shell” tracing the forward shock propagating at low speed into the ambient medium and an inner “main shell” tracing the jet–ambient interface (roughly delimited by the $f_a = 50\%$ border), where the wings of successive bowshocks pile-up. Both shells display a roughly parabolic or conical shape out to 20 000 au. Between these two shells is a slow cocoon of ambient material. Inside the main shell, we can discern several distinct “nested shells,” tracing the last bowshocks recently created by jet variability. This geometry is reminiscent of the “spider-like” structure observed at the base of the B5-IRS1 outflow, where an inner parabolic shell, with a jet shock at its apex, is nested inside the wide-angle low-velocity outflow cavity (Zapata et al. 2014).

Moreover, the mixing map (Fig. 5b) shows that a fraction of material from the surrounding core can go past the shock and mix with jet-originated material inside the main cavity up to the wings of the nested bowshocks. Some core-originated material can even reach particularly overdense areas bordering the jet walls, with n_H between 10^2 and 10^5 cm $^{-3}$. In the following, we assume that this core-originated material remains molecular for the purposes of computing the predicted synthetic emission diagrams.

Finally, Figs. 5c and d shows the radial and axial velocity maps, respectively. The new bowshocks encounter less resistance than those at earlier ages and develop broader wings, as the outflow cavity has been cleared up by tens of older bowshocks. Nevertheless, the characteristic kinematic pattern remains similar to early times, with enhanced- v_R in the bowshocks wings and a shear-like gradient of axial velocity v_z along the main shell at the jet–ambient interface. This velocity structure creates a characteristic “bell-shaped” pattern in transverse position-velocity diagrams, presented in Sect. 5.4.2.

5.3. Deceleration of the jet-driven shells

In contrast to a wind-driven shell in a flattened singular core, which expands at constant speed over time (Shu et al. 1991), a jet-driven shell is expected to decelerate. However, no analytical estimate of that deceleration exists in the case of a non-uniform ambient medium, making numerical simulations necessary.

Figure 6 shows the time evolution of the shell widths during the 10 000 yr-long simulation leading to the snapshot of

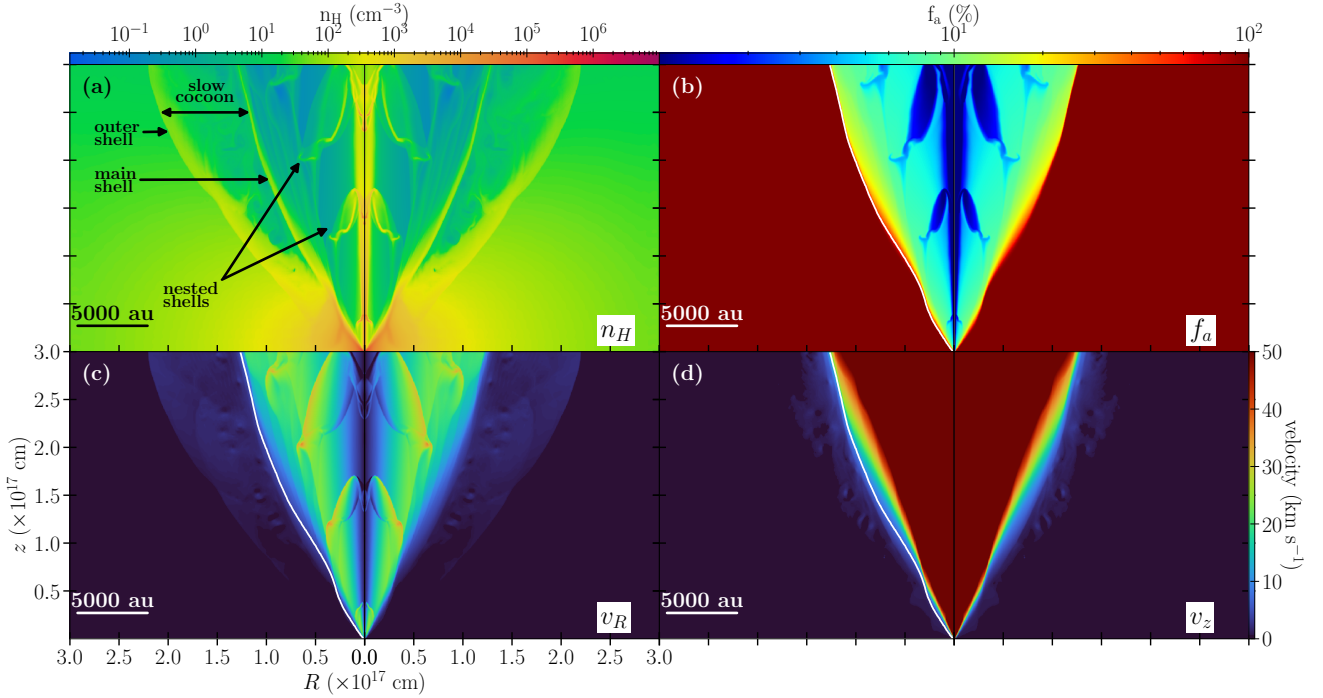


Fig. 5. Maps at $t = 10\,000$ yr of (a) hydrogen nuclei density n_H , (b) fraction of core-originated material f_a , (c) orthoradial velocity v_R , and (d) axial velocity v_z of the shell driven by a conical pulsed jet in a flattened singular core. Parameters are identical to model M_SAWT in Table A.1 except for a longer variability period $P = 300$ yr. Velocities in the colorbars are cropped to the range typically detected in CO outflow observations, namely between 0 and 50 km s^{-1} . The white contour in the left-half of panels of (b), (c), and (d) shows $f_a = 50\%$.

Fig. 5. We plot the full width as function of time at two different heights: $z = 800$ au (for comparison with Dutta et al. 2020), and $z = 20\,000$ au (top of the computational domain, after the jet head reaches it). We denote the corresponding shell widths as W_{800} and W_{20000} .

Figure 6 shows that the formation of two separate shells (denoted as the outer and main shells in Fig. 5) occurs around $t = 1000$ yr. Both shells are seen to decelerate at late times. Deceleration is stronger at lower altitudes, where the ambient core is denser. At $z = 800$ au, the main shell stops expanding after 6000 yr and reaches a final width $W_{800} \approx 2 \times 10^{16}$ cm = 1500 au. The corresponding final opening angle is $\alpha_{800} = 86^\circ$. This behavior is consistent with observations suggesting that the base opening angle of CO outflows stops increasing after $t \approx 8000$ yr, with a final value (uncorrected for inclination) $\alpha_{\text{obs}} \approx 90^\circ\text{--}100^\circ$ (Velusamy et al. 2014).

The widths W_{800} of the main shell at $z = 800$ au also fit very well within the observed range of flow widths at the same projected height (indicated by grey bands in Fig. 6), measured by Dutta et al. (2020) in a sample of 22 CO outflows in Orion. On large core scales of $z = 20\,000$ au = 0.1 pc, the main shell reaches a width $W_{20000} = 15\,000$ au at an age of 10^4 yr. This is similar to the observed CO outflow width at the same (deprojected) height in HH46-47 (Zhang et al. 2016), indicated in blue in Fig. 6. On intermediate scales of $z = 8000$ au, the main shell width at an age of 10^4 yr in our simulation is 9000 au (see Fig. 5). This is also in good agreement with cavity widths observed at the same (projected) distance in scattered light, lying in the range 1100–8500 au in 75% of cases (cf. semi-opening angles reported in Habel et al. 2021). Therefore, a jet driven into a flattened singular core seems able to reproduce typical observed outflow widths on both small and large scales for realistic long ages of $\geq 10\,000$ yr.

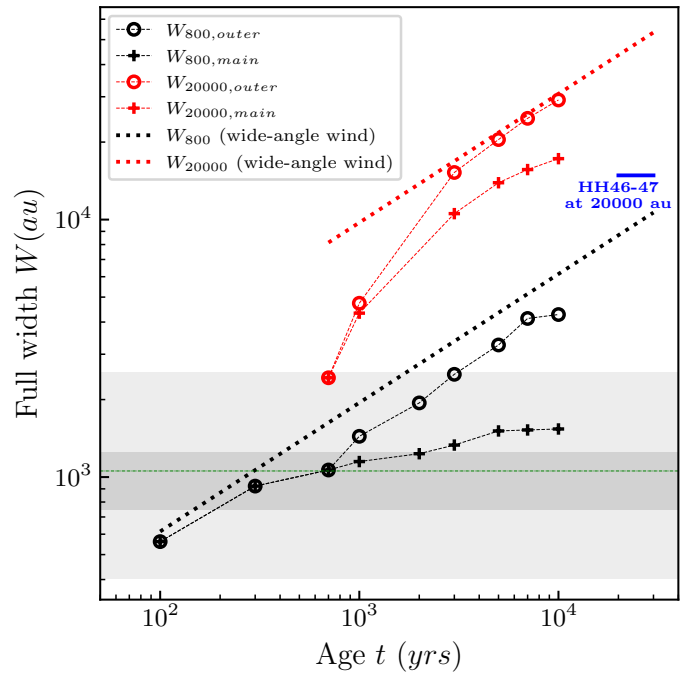


Fig. 6. Temporal evolution in the simulation of Fig. 5 of the full width of the main shell (jet–ambient interface, crosses) and outer shell (forward shock, circles) measured at altitudes $z = 800$ au (black) and $z = 20\,000$ au (red). Analytical predictions for the equivalent “modified X-wind” model of Lee et al. (2001) are shown as dotted black and red lines of slope $t^{1/2}$ (see text). The full range of CO outflow widths observed at $z = 800$ au by Dutta et al. (2020) is indicated by the light grey band (with second and third quartiles in darker grey, and median as a thin green line). The full width of the HH46-47 outflow at $z = 20\,000$ au, from Zhang et al. (2016), is shown in blue.

For comparison purposes, the dotted lines in Fig. 6 show the predicted evolution of shell widths at $z = 800$ and $20\,000$ au for the equivalent wide-angle “modified X-wind” model of Lee et al. (2001), which has the same mean axial velocity and total mass-flux as our jet and propagates in the same flattened singular core. In this model, the wind velocity drops away from the axis as $V_w = V_{w0} \cos \theta$, and the base of the shell is a parabola, $z = R^2/R_0$, expanding self-similarly over time as $R_0 = V_0 t$, where $V_0 = V_{w0} \sqrt{\eta}$ with η the (fixed) ratio of wind-to-ambient density in the equator. The shell width at any fixed height z is then given by $W_z = 2R = 2\sqrt{zV_0 t}$. In the equivalent wide-angle wind model considered here, $V_{w0} = 120 \text{ km s}^{-1}$ and $\eta = 2.2 \times 10^{-3}$ (Lee et al. 2001), yielding $V_0 = 5.6 \text{ km s}^{-1}$. Observed outflow shells fitted with the same analytical model³ have similar values of $V_0 \approx 1.5\text{--}9 \text{ km s}^{-1}$ (Lee et al. 2000; Zhang et al. 2019).

The black dotted line in Fig. 6 shows that while the wide-angle wind-driven shell predicts comparable widths to the jet-driven shell at early times ≤ 300 yr (as noted in Sect. 3), its self-similar expansion without deceleration exceeds observed CO outflow widths at $z = 800$ au (grey band in Fig. 6) after only 2000 yr, and the discrepancy increases over time as $t^{1/2}$. Recent simulations of X-wind-driven shells including magnetic fields in both the wind and the ambient medium predict similar shell widths at 500–1000 yr as this simple analytical model and confirm that the shell expands at constant rate in a self-similar fashion, $R \propto t$ (Shang et al. 2020). We note that this ongoing expansion is tightly linked to the adopted $1/r^2$ ambient density distribution (Shu et al. 1991). Steady wind-driven shells could form if the core has a shallower density gradient and if mixing is inefficient at the wind-core interface (Smith 1986; Liang et al. 2020).

5.4. Synthetic predictions

5.4.1. Longitudinal position-velocity diagrams

Figure 7 presents longitudinal position–velocity (PV) diagrams cut along the jet axis from our long-term simulation at $t = 10\,000$ yr, assuming various inclination angles, i , of the blueshifted lobe from the line of sight.

Most importantly, this figure shows that at ages typical of Class 0 outflows, negative velocities all vanish below an inclination angle of $i < 70^\circ$ from the line of sight. In particular, there is no more observable blue/red overlap at $i = 60^\circ$, unlike what has been predicted for jet-driven shells in uniform media (Lee et al. 2001).

This behavior is induced by the transverse deceleration of the main shell on late timescales, as discussed in Sect. 5.3. The slow expansion of the main shell restricts the sideways expansion of the bowshock wings propagating inside it, forcing them to adopt more forward-directed velocities. This may be seen in Fig. 8, where we plot the direction of velocity vectors in the outflow. Along the main shell, where bowshock wings pile up, velocity vectors are almost parallel to the shell walls. This produces much less blue-red overlap in the projection than is otherwise expected for a bowshock in a uniform medium. In the outer shell, which traces the forward shock expanding into the ambient medium, the velocity vectors are widely open (perpendicular to the shell) but the local expansion velocity is so low that the emission falls near rest velocity once it is projected.

Challenges to the notion of jet-driven shells producing too much blue-red overlap over a broad range of view angles thus

no longer appears justified when realistic long ages and ambient core stratifications are considered. A longitudinal PV cut extending up to 1.5×10^{17} cm from the source was recently obtained in the CARMA-7 outflow with ALMA (Plunkett et al. 2015), with both high resolution and high sensitivity.

A qualitative comparison with our predictions is presented in Fig. 9. Since the PV of CARMA-7 presents significant blue-red overlap, it is believed to be close to the plane of the sky, hence, we considered an inclination of $i = 85^\circ$ to the line of sight. The observed PV cut, reproduced in Fig. 9a, shows a striking quasi-periodic series of velocity peaks. The differences in dynamical timescales between successive identified velocity peaks yield an apparent period of variability in CARMA-7 of $\Delta\tau_{\text{dyn}} \approx 300$ yr (see Plunkett et al. 2015). However, for a quasi edge-on inclination, our synthetic PV diagrams with $P = 300$ yr in Fig. 7 predict a much wider knot spacing than observed in Fig. 9a. As noted by Plunkett et al. (2015), the value of $\Delta\tau_{\text{dyn}}$ may need to be corrected for projection effects by a typical factor 10. We thus present in Fig. 9 a model with jet variability period that is ten times shorter, namely, $P \approx 30$ yr.

Two synthetic PV diagrams are presented in Fig. 9: one including all material from jet and core (Fig. 9b) and the other including only core-originated material (Fig. 9c). Figure 9b is dominated by periodic sawtooth structures tracing the time variable jet and the sideways ejected material from its internal working surfaces (IWS). Figure 9c is dominated by structures with apparent “Hubble-law” acceleration, tracing ambient gas swept-up in the successive nested bowshock wings. We may remark that the jet and IWS remain faintly visible, through ambient gas dynamically entrained along the jet borders (cf. mixing map in Fig. 5b).

We find that the predicted structures in Fig. 9c are qualitatively similar to what is observed in CO emission in CARMA-7 (Fig. 9a). Since our model is very simplified (e.g., it does not include any jet precession), this qualitative agreement can be considered as promising. It also confirms that a suitable inclination-correction is essential to estimate the true period of velocity variations in a quasi edge-on outflow.

5.4.2. Transverse PV diagrams

Figures 10a, c show synthetic transverse PV diagrams for our 10000 yr-old simulation of an outflow with $P = 300$ yr (same simulation as in Fig. 5). We adopted an inclination angle $i = 55^\circ$ from the line of sight, the mean inclination of the HH46-47 jet determined by Hartigan et al. (2005). First, each diagram forms a characteristic “bell-like” shape, which peaks at high-velocity (the jet) and broadens smoothly down to rest velocity. This shape is a direct consequence of the deceleration of bowshock wings as they expand and interact inside the shell, which produces a velocity decreasing away from the jet axis. Second, while most of the mass is piled-up near rest velocity, and in the v_z “shear layer” along the shell walls (responsible for the two “horns” along the edges of the bell), bright ellipses are also present at intermediate velocities. Those ellipses trace intersections of the line of sight with individual bowshocks expanding inside the main shell.

These predicted characteristics (bell-shape with nested ellipses) bear striking qualitative resemblance with observed transverse PV cuts at high resolution and sensitivity, recently obtained with ALMA across the HH46-47 outflow by Zhang et al. (2019) and shown for comparison in Figs. 10b, d. The agreement appears even better than with models of wide-angle wind-driven shells (Zhang et al. 2019), which tend to overpredict

³ Lee et al. (2000) use different notations, $C = 1/R_0$ and $v_0 = 1/t$.

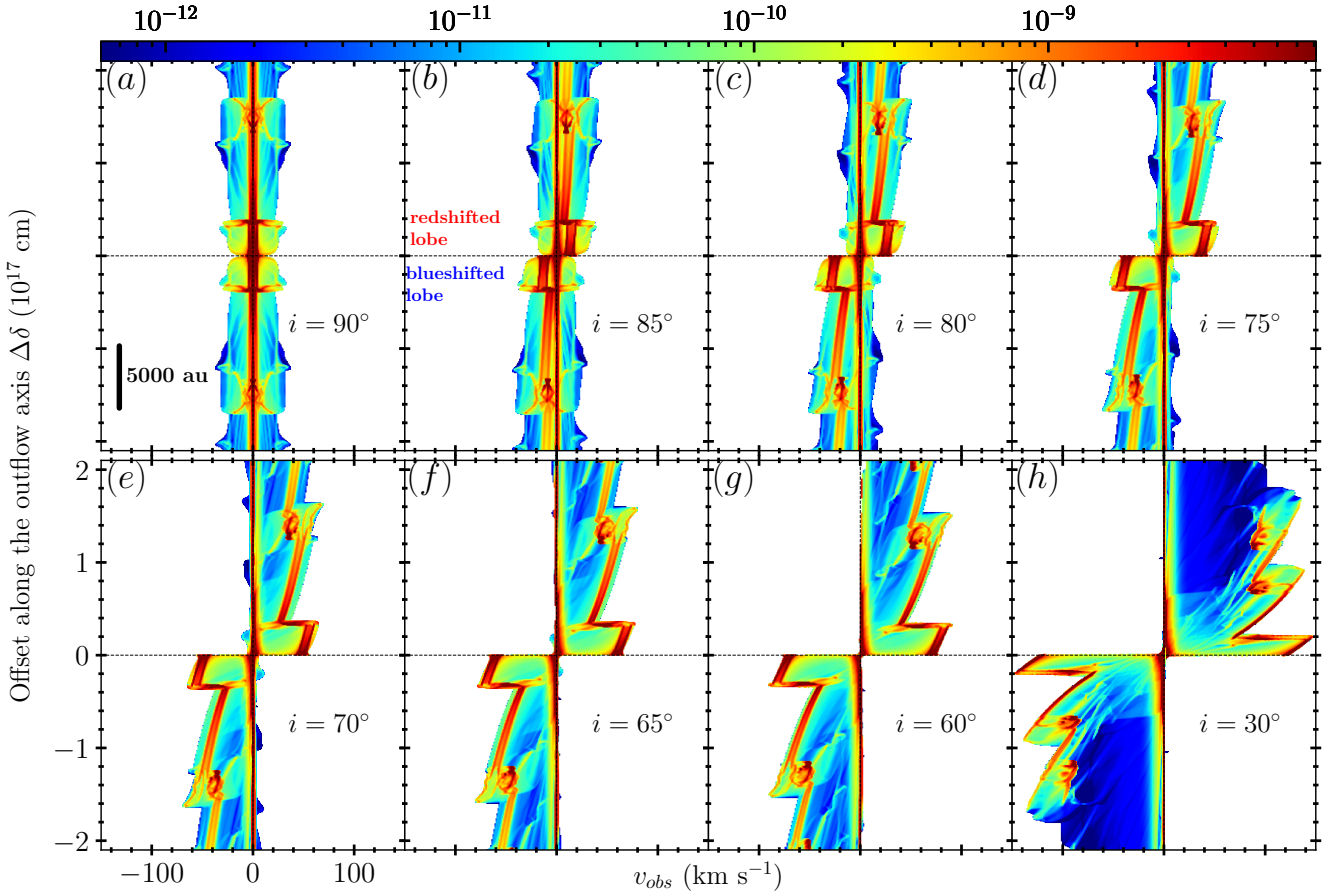


Fig. 7. Longitudinal position-velocity diagrams along the flow axis, inferred from the simulation in Fig. 5 at an age $t = 10\,000$ yr, for different inclination angles, i , from the line of sight, ranging from 90° (edge-on) to 30° .

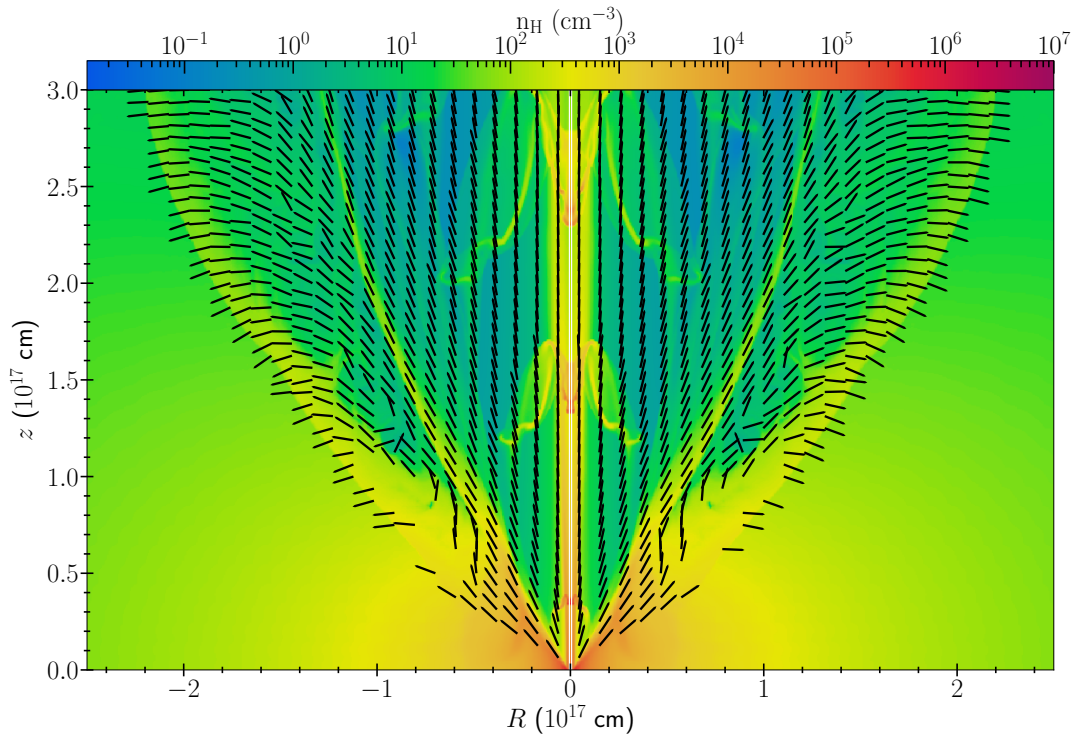


Fig. 8. Orientation of the velocity vectors for the $t = 10\,000$ yr-long simulation in Fig. 5, in the reference frame of the ambient core. Arrows are shown for velocities above 0.45 km s^{-1} , and are not scaled with the velocity modulus. Density is displayed in the background color image.

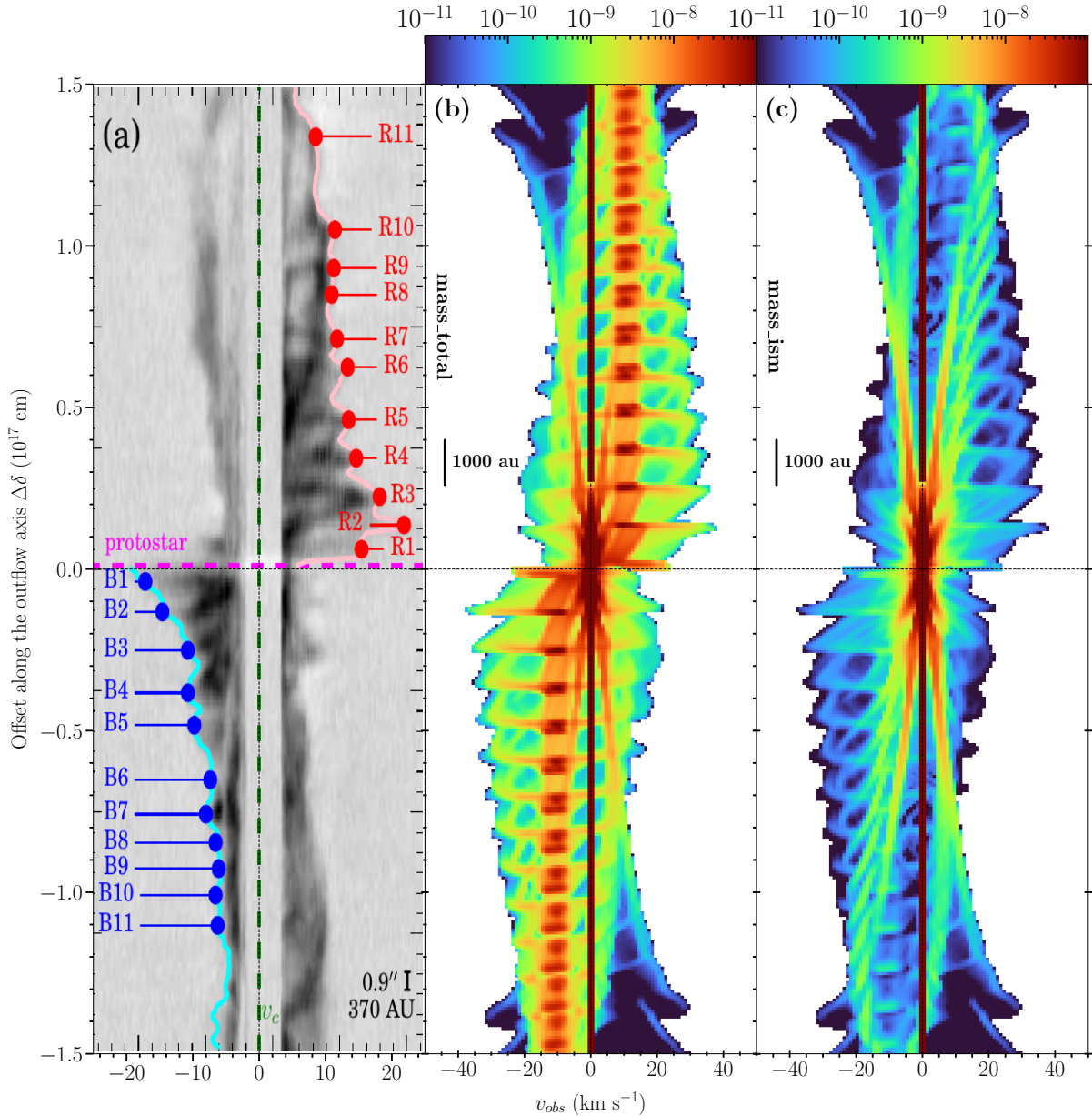


Fig. 9. Observed and modeled longitudinal position-velocity (PV) diagrams in CARMA-7. (a) Longitudinal PV diagram of CARMA-7 inside a 374 au-wide cut along the outflow axis, as observed in $^{12}\text{CO}(2-1)$ by Plunkett et al. (2015). (b) Synthetic longitudinal PV diagram along a 400 au-wide cut, at $t = 500$ yr, and inclination $i = 85^\circ$ from the line of sight. Parameters are the same as for the model shown in Fig. 5 except for a shorter jet variability period $P = 30$ yr. (c) Same as (b) but including only the core-originated material.

the outflow width at high projected velocities (see red ellipses on top of the observed PVs in Figs. 10b,d).

5.4.3. Mass-velocity distribution

As an additional diagnostic tool, Fig. 11 shows the mass-velocity (MV) distribution of entrained core material derived from the long term simulation in Fig. 5 at an age $t = 10\,000$ yr, assuming an inclination of $i = 55^\circ$ from the line of sight. This MV distribution is confronted to that derived by Zhang et al. (2016) from CO observations of the HH46-47 outflow, which is viewed at the same inclination angle.

Two observed MV distributions were computed by Zhang et al. (2016) and are plotted in Fig. 11: the first one (open symbols) was derived from ^{12}CO without correction for

optical depth. The shallow power-law slope $\gamma \approx -2$ is very typical of the slopes reported previously in other CO outflows, before optical-depth correction. The second observed MV distribution (filled symbols) was obtained after applying a velocity-dependent optical-depth correction to ^{12}CO and ^{13}CO data, and adding (optically thin) C^{18}O data at low velocities. Because optical depth increases at lower flow velocity, the corrected distribution exhibits a much steeper slope $\gamma \approx -3.4$ (in log-log). Similar steeper slopes have been obtained in other outflows after applying a velocity-dependent optical-depth correction, such as in B5-IRS1 (Yu et al. 1999).

Figure 11 shows a remarkably good qualitative agreement between the simulated and the observed MV distribution in HH46-47 after correction for optical depth, which should be closest to the true mass distribution in the outflow. This

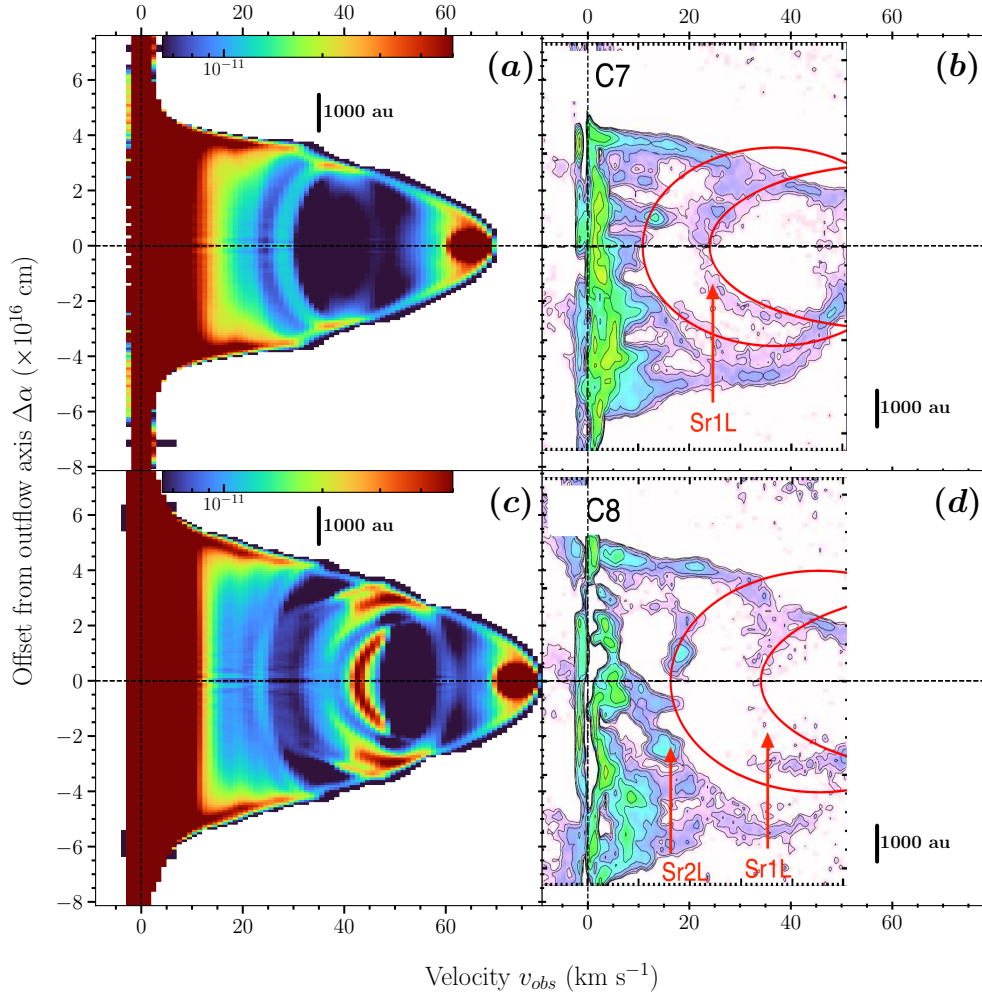


Fig. 10. Modeled and observed transverse position-velocity (PV) diagrams in HH46-47. *Left panels:* transverse position-velocity diagrams perpendicular to the outflow axis, inferred from the jet-driven shells simulation in Fig. 5 and Sect. 5.2, at $t = 10\,000$ yr inside 400 au-wide cuts at projected heights of (a) 6.6×10^{16} cm and (c) 8.9×10^{16} cm, with an outflow inclined by an angle $i = 55^\circ$ from the line of sight. Here only the core-originated material mass contribution is shown. *Right panels:* $^{12}\text{CO}(2-1)$ emission of HH46/47 along two 450 au-wide cuts at projected heights of (b) 8.1×10^{16} cm and (d) 1.0×10^{17} cm from the central source, with red ellipses showing best-fit models by wide-angle wind-driven shells. Adapted from Zhang et al. (2019).

agreement further reinforces the attractiveness of the jet-driven shell model at realistic long ages and with ambient stratification as a possible origin for CO outflows.

5.5. Model approximations

Here, we briefly discuss the main physics left out in our simulations and how it might affect the results. First, we considered an equilibrium atomic cooling curve, without following the out-of-equilibrium ionization and cooling behind shock fronts. Therefore, we cannot compute realistic synthetic emission maps in atomic and ionic lines, whose flux is proportional to the electron density. This approximation is sufficient, however, for our purpose of determining the overall shape, dynamics, and mass distribution in the dense shells of cooled post-shock gas. We also neglected chemistry, noting that CO dissociation only affects the observed mass distribution above 20 km s^{-1} (Downes & Cabrit 2003; Moraghan et al. 2008) and our comparisons with observations are made at lower velocities. Such approximations allow us to carry out for the first time, in a cost-effective way, long-term simulations up to 10^4 yr that can be compared with actual outflows observed with ALMA.

Overall, we neglected the infall motions. This allowed us to properly compare with simulations of outflows driven by X-winds into the same stratified singular cores (Lee et al. 2001; Shang et al. 2020), where infall is likewise neglected. In such cores, infall propagates inside-out at the ambient sound speed, a , and generates a shallower density distribution, $1/r^{1.5}$, inside the sonic radius, $r_{\text{inf}} = at$ (Terebey et al. 1984). Contrary to wind-driven flows where it can lead to a steady shell (Liang et al. 2020), a $1/r^{1.5}$ slope does not greatly reduce the width of jet-driven flows, as compared to $1/r^2$ (Moraghan et al. 2008). The main effect of infall would thus be to add shear, entrainment, and extra ram pressure at the base of the outer shell (cf. Liang et al. 2020, for the wind-driven case). For our simulation parameters, infall would occur inside $r_{\text{inf}} \approx 1000\text{ au} (a/0.5\text{ km s}^{-1}) \times (t/10^4\text{ yr})$ and, hence, it would affect only a small fraction of our full computational domain, extending up to 20 000 au.

Our simulation parameters do not explore the “long-period” regime where the ambient core would have time to partly refill the cavity in between jet outbursts. This interesting situation would occur if major outbursts happen only every few 10^4 yr, for instance, due to tidal interaction in wide eccentric binaries. The

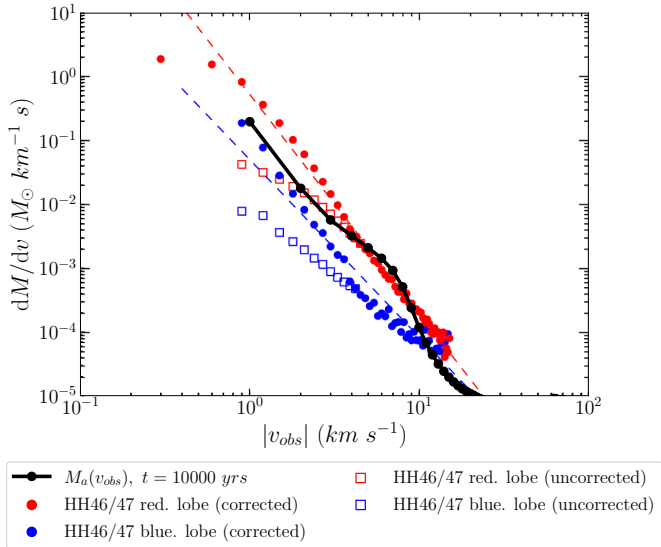


Fig. 11. Simulated mass-velocity (MV) distribution of core-originated material at $t = 10\,000$ yr from the jet-driven shell simulation in Figs. 5 and 10, inclined by $i = 55^\circ$ from the line of sight (connected black symbols). Blue and red symbols show observed MV distributions in the blueshifted and redshifted lobes of the HH46-47 outflow, as derived by Zhang et al. (2016). Open squares assume optically thin CO emission, while filled circles include a velocity-dependent correction for optical depth (see text). The dashed lines show power-laws of slope $\gamma = -3.4$ (red) and $\gamma = -2.7$ (blue).

observed spacing of jet knots in Class 0/I sources indicates much shorter variability timescales, however, with multiple periodic modes of decades, centuries, and thousands of years (Raga et al. 2012; Lee 2020). In addition, a recent study of infrared variability towards embedded protostars with *Spitzer*/IRAC presented the conclusion that Class 0 protostars undergo a major burst on average every 438 yr, with a 95% confidence interval of 161–1884 yr (Zakri et al. 2022). The long-period regime thus seems quite rare among the youngest, embedded Class 0/I objects that drive observable CO outflows.

Finally, we have neglected magnetic fields, both in the jet and in the ambient medium. Magnetic pressure in the jet would act to reduce the postshock compression and increase the cooling length, by typically an order of magnitude (Hartigan et al. 1994). This effect is observed directly in resolved internal shocks of stellar jets (Hartigan & Wright 2015). High-resolution radiative numerical simulations of pulsed magnetized jets show that the reduced cooling tends to broaden the nested bowshock shells, but the effect appears rather modest (de Colle & Raga 2006), justifying its omission here.

Conversely, a magnetic field in the ambient medium would tend to resist against the sideways shell expansion. A significant reduction in shell width compared to the purely hydrodynamic case requires, however, strong fields near equipartition (i.e., a ratio of thermal to magnetic pressure $\beta \approx 1$). This is demonstrated, for example, in the simulations of Shang et al. (2020) of X-wind-driven shells into cores of varying degrees of flattening and magnetization⁴. For the standard moderate core flattening,

⁴ The ratio of thermal to magnetic pressure in the core models of Shang et al. (2020) can be recovered as $\beta = 2\alpha_b^{-2}(v_A/a)^{-2}$ where $\alpha_b = [0, 0.1, 1]$ is their scaling parameter and (v_A/a) is the ratio of Alfvénic speed to sound speed in the magnetostatic solution of Li & Shu 1996 (Eq. (69)), which increases with the core flattening parameter n . A significant reduction in shell width compared to the hydrodynamical case

$n = 2$, adopted in the present work, the maximum reduction in shell width due to ambient magnetic field is only 25%, therefore, our predicted cavity shapes and dynamics should remain valid. We note that an added complexity at higher core magnetization, in the general case of non-zero rotation, would be the probable launching of a massive slow MHD wind from the Keplerian disk formed around the protostar (see e.g., Lesur 2021, and references therein). The interaction of an inner pulsed jet (or wide-angle X-wind) with an outer disk wind could significantly affect the formation of outflow cavities, but the long-term evolution has only been examined in the hydrodynamical case so far, to our knowledge (Tabone et al. 2018).

Concerning observational predictions, we focused here on signatures of the shell shapes, kinematics, and mass distribution at velocities below 20 km s^{-1} , which are well traced by low-excitation CO emission observable with ALMA. Our simulations may also be used to assess the detectability of warmer jet-originated material inside the cavity volume. From Fig. 5 we estimate that the nested shells (driven by each of the jet pulses) generate typical shock speeds of 30 km s^{-1} inside the cavity. The pre-shock density inside the cavity is $\approx 100\text{ cm}^{-3}$ at $z \leq 3000\text{ au}$, and drops off at higher altitudes. Using the atomic shock model grid of Hartigan et al. (1994), the maximum predicted surface brightness in [S II] for solar abundances is then $\approx 5 \times 10^{-6}\text{ erg s}^{-1}\text{ cm}^{-2}\text{ sr}^{-1}$. Such extended [S II] emission inside outflow cavities would be worthwhile to search for, but it might be difficult to isolate against the much brighter axial jet and scattered light from the cavity walls, especially since young protostars with powerful CO outflows are often located in regions of high optical extinction.

When the jet is dense enough to be partly molecular, another possible tracer of nested shells inside the main outflow cavity is H_2 ro-vibrational emission, the most spectacular example so far being the Class 0 outflow HH 212. Each large H_2 bowshock, produced by a major jet pulse, is seen to connect to a separate CO shell at the flow base, nested inside the main cavity (see Fig. 2 in Lee et al. 2015), a morphology consistent with our predictions for a pulsed jet-driven outflow. Modeling the H_2 line emission could be helpful to further discriminate between this scenario and the pulsed wide-angle wind model proposed by Zhang et al. (2019).

6. Conclusions

We confirm in this paper that the swept-up shell driven by a cylindrical pulsed jet opens much wider inside an ambient core with steeply decreasing density, than within a homogeneous core (which was the configuration commonly adopted until now for analytical models and most simulations of jet-driven bowshocks). At early times of a few hundred years, the jet-driven shell can open as wide as with a wide-angle X-wind, when considering the same flattened singular ambient core and the same injected mass-flux and velocity variability.

Then, we investigated the impact that several parameters in our model have on the general morphology, opening angle, and kinematics of jet-driven shells. The parameter which is by far the most impactful is the ambient core density, followed by the jet density and jet opening angle in a less impactful fashion. Within the range of values explored in this paper, the other parameters do not significantly affect these diagnostics.

is seen only in simulations with $n \geq 4$ and $\alpha_b = 1$, corresponding to midplane values of $\beta \leq 3.5$ that approach equipartition.

Finally, running a representative simulation up to $t = 10\,000$ yr reveals drastic changes in the long-term. After several hundred years, the initial shell splits into a slow parabolic outer shell fully made of core-original material (tracing the forward shock) and an inner, faster main shell tracing the jet-ambient interface, which stops expanding at the base after 8000 yr, unlike wide-angle wind-driven shells. This main shell encompasses a mixed-material cavity inside which successive bowshocks driven by the pulsed jet expand and slow down by interacting with previous ones, producing a strongly sheared velocity field parallel to the (roughly conical) main shell walls. Both the morphology and the velocity fields are very different from analytical predictions of ballistic jet bowshock models in uniform media (Ostriker et al. 2001).

The long-term simulation of our basic model shows none of the caveats of steady jet bowshocks in uniform media (excessive length to width ratio, excessive blue-red overlap, and overly low speeds at large shell widths). On the contrary, it shows very promising similarities with the most recent observations of Class 0 outflows observed at high resolution with ALMA, in terms of predicted shell widths, full opening angle ($\approx 90^\circ$ after 10^4 yr), longitudinal and transverse position-velocity cuts, and mass-velocity distribution (Dutta et al. 2020; Plunkett et al. 2015; Zhang et al. 2016, 2019). Some comparisons even show more resemblance to observations than the widely used wide angle “modified X-wind” model of Lee et al. (2001). This is the case for the moderate outflow widths at 800 au, the characteristic “bell-shape” of transverse PV cuts, and the steep mass-velocity relation after CO opacity correction.

More generally, this paper shows that a realistic modeling of the surrounding core density stratification, as well as long integration times of at least 10^4 yr, are both essential to reliably predict the properties of outflows driven by a pulsed jet, and to confront them with observations. In the future, we plan to extend our simulations to include chemistry, magnetic field, rotation, and precession to model specific observed protostellar outflows in more detail.

Acknowledgements. We are grateful to the anonymous referee for insightful suggestions that improved the paper, and to Doug Johnstone for supportive discussions and thoughtful comments. We acknowledge support by the Programme National Physique et Chimie du Milieu Interstellaire (PCMI) of CNRS/INSU with INC/INP co-funded by CEA and CNES. Part of the computations were carried out on the OCCIGEN cluster at CINES (<https://www.cines.fr/>) in Montpellier (project named Lut6216, allocation A0090406842 and A0100412483) and on the MesopSL cluster (<http://www.mesopsl.fr/>) of PSL University at Observatoire de Paris.

References

- Arce, H. G., Shepherd, D., Gueth, F., et al. 2007, in *Protostars and Planets V*, eds. B. Reipurth, D. Jewitt, & K. Keil, 245
- Arce, H. G., Borkin, M. A., Goodman, A. A., Pineda, J. E., & Halle, M. W. 2010, *ApJ*, **715**, 1170
- Béthune, W., Lesur, G., & Ferreira, J. 2017, *A&A*, **600**, A75
- Cabrit, S., Raga, A., & Gueth, F. 1997, in *Herbig-Haro Flows and the Birth of Stars*, eds. B. Reipurth, & C. Bertout, 182, 163
- Dalgarno, A., & McCray, R. A. 1972, *ARA&A*, **10**, 375
- de Colle, F., & Raga, A. C. 2006, *A&A*, **449**, 1061
- Dougados, C., Cabrit, S., Lavalley, C., & Ménard, F. 2000, *A&A*, **357**, A61
- Downes, T. P., & Cabrit, S. 2003, *A&A*, **403**, 135
- Dutta, S., Lee, C.-F., Liu, T., et al. 2020, *ApJS*, **251**, 20
- Federrath, C., Schrön, M., Banerjee, R., & Klessen, R. S. 2014, *ApJ*, **790**, 128
- Ferreira, J., & Deguiran, R. 2013, *High Energy Density Phys.*, **9**, 67
- Frank, A., Ray, T. P., Cabrit, S., et al. 2014, in *Protostars and Planets VI*, eds. H. Beuther, R. S. Klessen, C. P. Dullemond, & T. Henning, 451
- Habel, N. M., Megeath, S. T., Booker, J. J., et al. 2021, *ApJ*, **911**, 153
- Hartigan, P., & Wright, A. 2015, *ApJ*, **811**, 12
- Hartigan, P., Morse, J. A., & Raymond, J. 1994, *ApJ*, **436**, 125
- Hartigan, P., Heathcote, S., Morse, J. A., Reipurth, B., & Bally, J. 2005, *AJ*, **130**, 2197
- Ireland, L. G., Zanni, C., Matt, S. P., & Pantolmos, G. 2021, *ApJ*, **906**, 4
- Kaastra, J. S., & Mewe, R. 2000, in *Atomic Data Needs for X-ray Astronomy*, eds. M. A. Bautista, T. R. Kallman, & A. K. Pradhan, 161
- Keppens, R., Teunissen, J., Xia, C., & Porth, O. 2021, *Comput. Math. Applic.*, **81**, 316
- Krumholz, M. R., & Federrath, C. 2019, *Front. Astron. Space Sci.*, **6**, 7
- Lee, C.-F. 2020, *A&ARv*, **28**, 1
- Lee, C.-F., Mundy, L. G., Reipurth, B., Ostriker, E. C., & Stone, J. M. 2000, *ApJ*, **542**, 925
- Lee, C.-F., Stone, J. M., Ostriker, E. C., & Mundy, L. G. 2001, *ApJ*, **557**, 429
- Lee, C.-F., Hirano, N., Zhang, Q., et al. 2015, *ApJ*, **805**, 186
- Lesur, G. R. J. 2021, *A&A*, **650**, A35
- Li, S. 2005, *J. Comput. Phys.*, **203**, 344
- Li, Z.-Y., & Shu, F. H. 1996, *ApJ*, **472**, 211
- Liang, L., Johnstone, D., Cabrit, S., & Kristensen, L. E. 2020, *ApJ*, **900**, 15
- MacDonald, J., & Bailey, M. E. 1981, *MNRAS*, **197**, 995
- Masson, C. R., & Chernin, L. M. 1993, *ApJ*, **414**, 230
- Matzner, C. D., & McKee, C. F. 1999, *ApJ*, **526**, L109
- Moraghan, A., Smith, M. D., & Rosen, A. 2008, *MNRAS*, **386**, 2091
- Motte, F., & André, P. 2001, *A&A*, **365**, 440
- Ostriker, E. C., Lee, C.-F., Stone, J. M., & Mundy, L. G. 2001, *ApJ*, **557**, 443
- Plunkett, A. L., Arce, H. G., Mardones, D., et al. 2015, *Nature*, **527**, 70
- Porth, O., Xia, C., Hendrix, T., Moschou, S. P., & Keppens, R. 2014, *ApJS*, **214**, 4
- Raga, A., & Cabrit, S. 1993, *A&A*, **278**, 267
- Raga, A. C., Canto, J., Binette, L., & Calvet, N. 1990, *ApJ*, **364**, 601
- Raga, A. C., Rodríguez-González, A., Noriega-Crespo, A., & Esquivel, A. 2012, *ApJ*, **744**, L12
- Rohde, P. F., Walch, S., Seifried, D., et al. 2019, *MNRAS*, **483**, 2563
- Santiago-García, J., Tafalla, M., Johnstone, D., & Bachiller, R. 2009, *A&A*, **495**, 169
- Schure, K. M., Kosenko, D., Kaastra, J. S., Keppens, R., & Vink, J. 2009, *A&A*, **508**, 751
- Shang, H., Allen, A., Li, Z.-Y., et al. 2006, *ApJ*, **649**, 845
- Shang, H., Krasnopolsky, R., Liu, C.-F., & Wang, L.-Y. 2020, *ApJ*, **905**, 116
- Shu, F. H., Ruden, S. P., Lada, C. J., & Lizano, S. 1991, *ApJ*, **370**, L31
- Shu, F. H., Najita, J., Ostriker, E. C., & Shang, H. 1995, *ApJ*, **455**, L155
- Smith, M. D. 1986, *MNRAS*, **223**, 57
- Suttner, G., Smith, M. D., Yorke, H. W., & Zinnecker, H. 1997, *A&A*, **318**, 595
- Tabone, B., Raga, A., Cabrit, S., & Pineau des Forêts, G. 2018, *A&A*, **614**, A119
- Terebey, S., Shu, F. H., & Cassen, P. 1984, *ApJ*, **286**, 529
- van der Marel, R. P., Kallivayalil, N., & Besla, G. 2009, in *The Magellanic System: Stars, Gas, and Galaxies*, eds. J. T. Van Loon, & J. M. Oliveira, 256, 81
- van Marle, A. J., & Keppens, R. 2011, *Computers and Fluids*, **42**, 44
- Velusamy, T., & Langer, W. D. 1998, *Nature*, **392**, 685
- Velusamy, T., Langer, W. D., & Thompson, T. 2014, *ApJ*, **783**, 6
- Völker, R., Smith, M. D., Suttner, G., & Yorke, H. W. 1999, *A&A*, **343**, 953
- Yu, K. C., Billawala, Y., & Bally, J. 1999, *AJ*, **118**, 2940
- Zakri, W., Megeath, S. T., Fischer, W. J., et al. 2022, *ApJ*, **924**, L23
- Zapata, L. A., Arce, H. G., Brassfield, E., et al. 2014, *MNRAS*, **441**, 3696
- Zhang, Y., Arce, H. G., Mardones, D., et al. 2016, *ApJ*, **832**, 158
- Zhang, Y., Arce, H. G., Mardones, D., et al. 2019, *ApJ*, **883**, 1

Appendix A: Effect of variables with lower jet density

In this appendix, we redo the process of Sect. 4, but starting from a reference model with a jet base density that is two lower by orders of magnitude: $\rho_{j0} = 1.8 \times 10^{-19} \text{ g cm}^{-3}$. In this way, we can further probe the effects of the base jet density on the morphology and kinematics of the driven shells. We also test the robustness of the conclusions we got from Sect. 4 at other jet density values.

Thus, additionally to the reference model, we launch seven modified models, each having the same parameters as the reference model except for a single one. Those models are :

(i) M_DENSA: with an ambient density scaling $\rho_{a,0}$ of $1.6 \times 10^{-20} \text{ g cm}^{-3}$ instead of $1.6 \times 10^{-18} \text{ g cm}^{-3}$;

(ii) M_THETA: with a jet semi-opening angle θ_j of 7° instead of 3° ;

(iii) M_DENSJ: with a jet base density ρ_{j0} 100 times larger than the reference case;

(iv) M_VARAMP: with a variability semi-amplitude ΔV of 90 km/s instead of 60 km/s;

(v) M_PER: with a variability period $P = 300$ yr instead of 115 yr;

(vi) M_SAWT: with a sawtooth instead of sinusoidal velocity variability profile ;

(vii) M_RAD: with an initial jet radius R_j of 20 au instead of 50 au.

Figure A.1 plots and compares the inferred shell shapes at $t = 700$ yr for the reference and modified models. Table A.1 summarizes the parameters of the simulations, and lists the full opening angle at 800 au, α_{800} , and full shell widths at $z = 800$ au and 12700 au (W_{800} and W_{12700}) measured at $t = 700$ yr in each model. The effect of parameters changes on the outflow structure are discussed in Sect. 4.3.

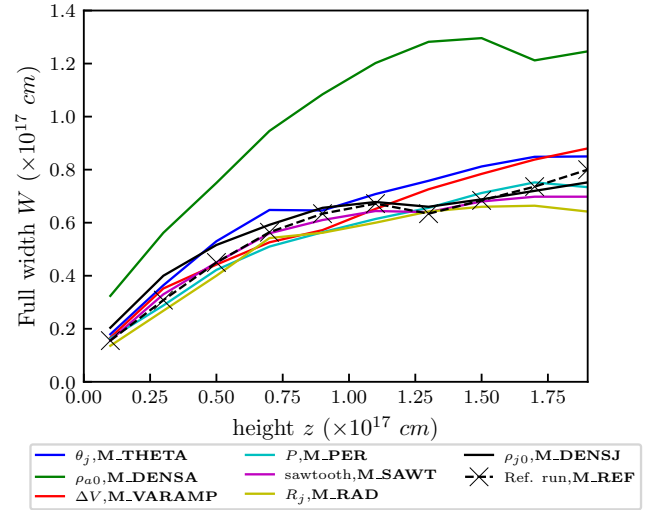


Fig. A.1: Full shell width $W(z)$ at $t = 700$ yr as a function of altitude z for the models in Table A.1, with jet densities 100 times smaller than in Fig. 4. Colored curves have one parameter varied from the reference run, among the ambient core base density, ρ_{a0} , jet semi-opening angle, θ_j , initial jet base density, ρ_{j0} , semi-amplitude of variability, ΔV , period, P , type of variability profile (sawtooth instead of sinusoidal), or jet radius, R_j .

Table A.1: Parameters of conical pulsed medium-density jet simulations with the resulting opening angles and full widths

<i>Fixed parameters</i>	
mean jet velocity	$v_0 = 120 \text{ km/s}$
jet density variation	$\rho_j(t) = \rho_{j0} [v_0/v_j(t)] \times (R_j^2 + z_0^2)(R^2 + [z + z_0]^2)^{-1}$, with $z_0 = R_j/\tan\theta_j$ (constant mass-flux)
jet temperature	$T_j = 100 \text{ K}$
ambient core temperature	$T_a = 100 \text{ K}$
core density profile	Flattened singular core $\rho_a(\mathbf{r}) = \rho_{a0} \sin^2\theta r_0^2 (r^2)^{-1}$, with $r_0 = 2.5 \times 10^{15} \text{ cm}$
radiative cooling function	$\Lambda(100 \text{ K} \leq T < 10^4 \text{ K})$ from Dalgarno & McCray (1972) $\Lambda(T \geq 10^4 \text{ K})$ from Schure et al. (2009)
simulation domain	$(R, z) = (7.0 \times 10^{16} \text{ cm}, 1.9 \times 10^{17} \text{ cm}) = (4679 \text{ au}, 12700 \text{ au})$
number of cells	$n_R \times n_z = 56 \times 152$ at AMR level 1
maximal AMR level	5
maximum resolution	$\Delta R = \Delta z = 7.8 \times 10^{13} \text{ cm} = 5.2 \text{ au}$ at AMR level 5
snapshot age	700 yr

Parameter	Reference Model M_REF	Modified parameter ^a	Modified Model name	α_{800} ^b ($^\circ$)	\mathbf{W}_{800} ^c (10^{16} cm)	\mathbf{W}_{12700} ^d (10^{16} cm)
core base density ρ_{a0}	$1.6 \times 10^{-18} \text{ g cm}^{-3}$	$1.6 \times 10^{-20} \text{ g cm}^{-3}$	M_DENSA	112	3.5	12.4
jet semi opening angle θ_j	3°	7°	M_THETA	81	2.0	8.4
jet base initial density ^e ρ_{j0}	$1.8 \times 10^{-19} \text{ g cm}^{-3}$	$1.8 \times 10^{-17} \text{ g cm}^{-3}$	M_DENSJ ^f	88	2.3	7.6
semi-amplitude ΔV	60 km/s	90 km/s	M_VAMP	77	1.9	8.8
jet variability period P	115 yr	300 yr	M_PER	74	1.8	7.4
jet variability profile $h(t)$	$1 + \frac{\Delta V}{v_0} \sin \frac{2\pi t}{P}$	$1 + \frac{\Delta V}{v_0} \{1 - 2 \cdot \text{mod}(\frac{t}{P}, 1)\}$	M_SAWT	74	1.8	7.0
jet radius R_j	$7.5 \times 10^{14} \text{ cm}$	$3.0 \times 10^{14} \text{ cm}$	M_RAD	65	1.5	6.4

^a In each modified model, only one parameter at a time is changed with respect to the reference model.

^b Shell full opening angle at $z = 800 \text{ au}$. We obtain $\alpha_{800} = 72^\circ$ for the reference model.

^c Full shell width at $z = 800 \text{ au}$. We obtain $\mathbf{W}_{800} = 1.7 \times 10^{16} \text{ cm}$ for the reference model.

^d Full shell width at $z = 12700 \text{ au}$ (top of the grid). We obtain $\mathbf{W}_{12700} = 8.0 \times 10^{16} \text{ cm}$ for the reference model.

^e Medium jet density case, yielding a one-sided mass-flux $\dot{M} = 6 \times 10^{-8} M_\odot/\text{yr}$ for the reference values of θ_j and R_j
^f This model is equivalent to H_REF.